

TEN MILLION DEGREE GAS IN M 17 AND THE ROSETTE NEBULA: X-RAY FLOWS IN GALACTIC HII REGIONS

LEISA K. TOWNSLEY¹, ERIC D. FEIGELSON^{1,2}, THIERRY MONTMERLE², PATRICK S. BROOS¹, YOU-HUA CHU³, AND GORDON P. GARMIRE¹*Draft version October 31, 2018*

ABSTRACT

We present the first high-spatial-resolution X-ray images of two high-mass star forming regions, the Omega Nebula (M 17) and the Rosette Nebula (NGC 2237–2246), obtained with the *Chandra X-ray Observatory* Advanced CCD Imaging Spectrometer (ACIS) instrument. The massive clusters powering these HII regions are resolved at the arcsecond level into >900 (M 17) and >300 (Rosette) stellar sources similar to those seen in closer young stellar clusters. However, we also detect soft diffuse X-ray emission on parsec scales that is spatially and spectrally distinct from the point source population. The diffuse emission has luminosity $L_x \simeq 3.4 \times 10^{33}$ ergs s⁻¹ in M 17 with plasma energy components at $kT \simeq 0.13$ and $\simeq 0.6$ keV (1.5 and 7 MK), while in Rosette it has $L_x \simeq 6 \times 10^{32}$ ergs s⁻¹ with plasma energy components at $kT \simeq 0.06$ and $\simeq 0.8$ keV (0.7 and 9 MK). This extended emission most likely arises from the fast O-star winds thermalized either by wind-wind collisions or by a termination shock against the surrounding media. We establish that only a small portion of the wind energy and mass appears in the observed diffuse X-ray plasma; in these blister HII regions, we suspect that most of it flows without cooling into the low-density interstellar medium. These data provide compelling observational evidence that strong wind shocks are present in HII regions.

Subject headings: HII regions – open clusters and associations: individual (NGC 2244, NGC 6618) – stars: activity – stars: early-type – stars: high mass – stars: pre–main-sequence – X-rays: stars

1. INTRODUCTION

One of the great successes in astrophysics during the mid-20th century was the development of a detailed explanation for HII regions and other bright emission-line nebulae (Menzel 1937; Strömgren 1939; Aller 1956). A hot star with strong ultraviolet radiation produces an expanding ionization front which spreads into the surrounding medium. Early studies concentrated on the ionization front, its associated shock, and various other considerations such as magnetic fields, turbulence, dynamical instabilities, and radiation pressure on dust particles (Mathews & O’Dell 1969).

These efforts omitted the potential effects of the powerful winds of OB stars, which were not known until the discovery of ultraviolet P Cygni profiles by Morton (1967). Winds make a relatively small contribution to the overall energy budget of HII regions: the wind mechanical luminosity ranges from 0.3% (B0 V) to 2% (O4 V) of the ionizing continuum luminosity (Panagia 1973; Howarth & Prinja 1989). However, they can easily dominate the dynamics of the nebula by evacuating a hot cavity with characteristic temperatures of $T \sim 10^7 - 10^8$ K, and producing two-fluid shocks which lie within the ionization shocks in the cooler $T \sim 10^4$ K HII region (e.g. Pikel’ner 1968; Dyson & de Vries 1972; Weaver et al. 1977). See Lamers & Cassinelli (1999) for details of these models and a historical review of stellar wind studies.

In the interstellar bubble model developed by Weaver et al. (1977), a single 10^6 yr old O7 star with a terminal wind velocity $v_w = 2000$ km s⁻¹ and mass loss rate $\dot{M} = 1 \times 10^{-6} M_\odot$ yr⁻¹, surrounded by a uniform interstellar medium of density $n_o = 1$ cm⁻³, will have an innermost region where the wind freely expands and cools, followed by a hot $T \sim 10^6$ K region starting at the wind termination shock 6 pc from the star and extending

to an outer shock at 27 pc. This X-ray emitting region occupies most of the volume of the bubble and consists mostly of evaporated interstellar material rather than wind material. Outside this hot region lies a thin shell of swept-up interstellar matter at $T \simeq 10^4$ K, beyond which lies the much larger standard photoionized HII region.

The fate of OB winds in HII regions may not be as simple as described in the Weaver et al. interstellar bubble model. The wind-swept bubble can be larger or smaller than the ionized HII region, and nonadiabatic dissipation due to conduction, mixing, turbulence and magnetic fields at the shock fronts may affect the properties of the coronal region (Capriotti & Kozminski 2001). Another possibility is that the winds are slowed by the entrainment of dense clumps of interstellar matter before the termination shock. In such mass-loaded stellar winds, extensively studied by Dyson and his collaborators (Pittard, Hartquist, & Dyson 2001, and references therein), the flow is heated to X-ray temperatures closer to the star and the outer shock is weaker. Finally, it is possible that no X-ray emission will emerge at all if the surrounding medium is too fragmented (McKee, van Buren, & Lazareff 1984) or wind energy is slowly dissipated in a thick turbulent mixing layer (Kahn & Breitschwerdt 1990).

Despite three decades of theoretical discussions of hot cavities produced by OB stellar winds, only a few detailed predictions of observable X-ray properties of the shocked wind have been made. Dorland & Montmerle (1987) investigated the dissipation of a $v_w = 1000$ km s⁻¹ O star wind, including conduction processes, predicting an X-ray to wind kinetic luminosity ratio $L_x/L_w \sim 10^{-5}$ and X-ray temperatures around 2 keV (23 MK) with a nonthermal hard-energy tail. Comerón (1997) presents a two-dimensional hydrodynamical model of

¹ Department of Astronomy & Astrophysics, 525 Davey Laboratory, Pennsylvania State University, University Park, PA 16802

² Service d’Astrophysique, Centre d’Études de Saclay, 91191 Gif-sur-Yvette, France

³ Astronomy Department, University of Illinois at Urbana-Champaign, 1002 West Green Street, Urbana, IL 61801

an O star residing near the edge of an interstellar cloud, showing the evolution of X-ray morphology as the wind cavity produces a blow-out into the diffuse interstellar medium. Strickland & Stevens (1999) give a hydrodynamical calculation for a very young ($t \sim 10^4$ yr) O star completely embedded in a dense cloud and find that, while most of the emission from the wind termination shock is in the EUV band, the wind-swept interior emits X-rays up to several keV in temperature. Cantó, Raga, & Rodríguez (2000) present a 3-dimensional hydrodynamical calculation of a rich ensemble of O stars allowing for mass loading, wind collisions, and shocks, but without an encounter with a surrounding cloud. This results in an inhomogeneous X-ray structure with $L_x \simeq 6 \times 10^{35}$ ergs s^{-1} and $T \simeq 2 \times 10^7$ K concentrated in the inner $r \simeq 0.3$ pc of the stellar cluster.

On the observational side, until very recently there had been no unambiguous report of diffuse X-ray emission from HII regions although it has been detected around some isolated Wolf-Rayet stars, within planetary nebulae, and in starburst superbubbles (see reviews by Mac Low 2000; Chu, Guerrero, & Gruendl 2002; Chu 2002; Chu, Gruendl, & Guerrero 2003). Using the *Einstein Observatory*, Seward & Chlebowski (1982) found extended soft X-rays over tens of parsecs in the Carina Nebula with $L_x \simeq 2 \times 10^{35}$ ergs s^{-1} , in addition to a score of individual OB/W-R stellar sources. However, this is a large and old star formation region with many supergiants, so it is possible that this extended emission is dominated by past supernova remnants. Leahy (1985) suggested a diffuse origin for emission within the Rosette Nebula seen with *Einstein*, further discussed by Dorland & Montmerle (1987), but a later higher-resolution *ROSAT* study concluded that this unresolved component was due to the integrated emission from many lower mass pre-main sequence stars (Berghöfer & Christian 2002). In an *Einstein* survey of LMC HII regions, Chu & Mac Low (1990) found several with X-ray emission at levels around $10^{35} - 10^{36}$ ergs s^{-1} , an order of magnitude higher than expected from the wind shocked bubble, which they attribute to off-center supernova remnants hitting the outer shells.

The difficulties encountered in past efforts to detect the $T \sim 10^6 - 10^7$ K gas in HII region wind-blown bubbles arise from the complex environment in the X-ray band. A high-mass star forming region 1 – 10 pc in extent will have thousands of lower-mass pre-main sequence stars each emitting $10^{28} - 10^{31}$ ergs s^{-1} , individual OB and Wolf-Rayet stars each emitting $10^{30} - 10^{34}$ ergs s^{-1} , possibly supernova remnants and superbubbles emitting $10^{34} - 10^{37}$ ergs s^{-1} , and possibly X-ray binary systems from past episodes of star formation each emitting $10^{33} - 10^{40}$ ergs s^{-1} (Feigelson 2001). These observational difficulties are largely overcome with the *Chandra X-ray Observatory*, where the mirrors give unprecedented sub-arcsecond spatial resolution and the ACIS instrument has the very low background necessary to study faint diffuse emission. *Chandra* thus provides the best opportunity to date to resolve the extended, low surface brightness wind-blown bubbles from the plethora of compact stellar X-ray sources expected in high-mass star forming regions. Several reports of wind-generated diffuse X-ray emission from HII regions are thus emerging from recent *Chandra* observations.

We report here on *Chandra* studies of two bright, nearby ($d \sim 1.5$ kpc), and well-studied HII regions: M 17 and the Rosette Nebula. In M 17, we show that the *Chandra* image reveals strong diffuse X-rays both within and expanding asym-

metrically from the stellar cluster, in addition to several hundred young stars. Preliminary results for M 17 were presented in Townsley et al. (2003). In the Rosette, we see relatively faint X-ray emission suffusing the hollow core of the HII gas, together with a rich stellar population⁴. These observations, and the astrophysical analysis derived from them, represent the strongest observational evidence to date for X-ray emission from the wind-blown cavities of HII regions; the morphological and spectral properties of the hot plasma should constrain some of the theoretical uncertainties concerning the fate of OB winds and the resulting evolution of HII regions.

The paper starts with an overview of each HII region (§2) and then presents our observations and results from data analysis (§3). The complex morphologies of the X-ray images are reviewed in §4 and the physical nature of the emitting gas is derived in §5. Several possible origins of the diffuse emission are considered in §6 and the wind shock model is discussed in more detail in §7. The two regions studied here are placed into a wider context in §8. The paper ends with general comments about the fate of O star winds in HII regions (§9).

2. OBSERVATIONAL BACKGROUND ON THE HII REGIONS

2.1. M 17

The HII region M 17 (= Omega Nebula = W 38, at $(l, b) = (15.1, -0.7)$) is visually very bright and has been extensively studied for two centuries. It is illuminated by the massive stellar cluster NGC 6618, the center of which consists of a ring of seven O stars $\sim 1'$ in diameter located behind substantial obscuring material, with $A_V \sim 8$ mag (Hanson, Howarth, & Conti 1997). The cluster core radius is $\sim 5.5'$ (2.6 pc) and its outer radius is $\sim 12.5'$ (5.8 pc) (Lyngå 1987). The earliest O stars are an O4–O4 binary called Kleinmann’s Anonymous Star (Kleinmann 1973). The nebula is the second brightest thermal radio source in the sky (after Orion A) and is situated at the edge of a massive and dense molecular cloud; its appearance varies significantly as a function of wavelength because of spatially complex extinction.

A global geometric model of the M 17 complex is presented by Tsivilev & Krasnov (1999, their Figure 4); they note its similarity to the pressure-driven bubble model of Clayton et al. (1985), who in turn note that the highly asymmetric bubble they see agrees with the models of Dyson (1977) and Rozyczka & Tenorio-Tagle (1985) for the formation of a wind-blown bubble in the density gradient present at the edge of a molecular cloud. Tsivilev & Krasnov (1999) describe a bowl-shaped region ~ 2 pc across and expanding westward into the molecular cloud, with a much larger, unobscured optical HII region spreading into the low-density medium at the eastern edge of the cloud. The complex resembles the Orion Nebula/KL region seen nearly edge-on (Meixner et al. 1992): the bowl-shaped ionization blister is eroding the edge of the clumpy molecular cloud and triggering massive star formation, as evidenced by an ultra-compact HII region and luminous protostars. Velocity studies show an ionized shell in the middle of the nebula with a diameter of 8 pc ($\sim 17'$) (Clayton et al. 1985). The ionization front encounters the molecular cloud at two photodissociation regions, known as the northern and southern bars, about $20'$ in length and at an apparent angle of $\sim 45^\circ$ to each other. These dominate the radio continuum and emission line images of the region (Figure 1a). The bowl is oriented somewhat past edge-on to our line-of-sight, with the blow-out moving away from

⁴ See the press release at http://chandra.harvard.edu/press/01_releases/press_090601wind.html.

us.

In the radio band unaffected by extinction, low resolution and low frequency studies with the Very Large Array show an optically thick, bright region associated with bright H α emission truncated abruptly to the west. This is embedded within an optically thin region extending over $30' \times 40'$ ($\sim 14 \times 19$ pc) which represents the full extent of ionized material (Subrahmanyan & Goss 1996). The electron temperature is $T_e \sim 8000$ K. At higher resolution and frequencies, where the HII gas is optically thin, the emission is dominated by the bars (Figure 1a; Felli, Massi, & Churchwell 1984; Brogan & Troland 2001). The gas in the bars has electron density $n_e \sim 10^3$ cm $^{-3}$ but is not uniform, with clumps of higher density. The Lyman continuum flux necessary to excite the bars is consistent with the ultraviolet emission from the O4–B0 stellar cluster, confirming a simple photoionization origin for the radio-emitting gas.

In the visual band, the *Digital Sky Survey* (DSS) red image is dominated by H α nebulosity from the northern bar, but emission from the southern bar and ionizing cluster is largely absorbed (Figure 1b). At low surface brightness, the DSS image shows H α extending over $\sim 20' \times 20'$ with features closely correlated with the low frequency radio structures where extinction is low; particularly noticeable are a few large arc-shaped features. Optical spectroscopy has shown high-excitation optical emission lines rarely seen in other HII regions (Glushkov 1998). Near-infrared images suffer less obscuration and clearly display line emission from the bars seen in the radio, as well as the exciting stellar cluster (Figure 1c). Recent deep near-infrared observations reveal a circular cavity in the gas around the exciting cluster as well as many cluster members and embedded young stars in the surrounding dark cloud (Ando et al. 2002; Jiang et al. 2002).

In the X-ray band, M 17 was observed with *ROSAT* for 6.7 ks; the findings have just recently been published (Dunne et al. 2003, hereafter Dunne03). We show the *ROSAT* proportional counter (PSPC) ‘full band’ (0.1–2.4 keV) image, slightly smoothed with a Gaussian kernel, in Figure 1d; contours from this exposure are superposed on a new H α image in Dunne03 (their Figure 1). The X-ray image shows strong emission around the core of the ionizing cluster and an elongated structure extending $20'$ to the east-southeast, parallel to the northern bar and filling the optically thick part of the DSS image. Extended, fainter emission matching the diffuse H α emission is visible towards the east and north; no limb-brightening is seen. Dunne03 found $kT = 0.66$ – 0.78 keV ($T = 7.7$ – 9.1 MK) and $N_H = 1$ – 5×10^{20} cm $^{-2}$ for this emission, with electron densities $n_e \sim 0.06$ – 0.09 cm $^{-3}$ and a total luminosity (in the 0.1–2.4 keV band) of $L_x \sim 2 \times 10^{33}$ ergs s $^{-1}$. For the area of bright X-ray emission close to the ionizing cluster, the *ROSAT* spectrum was not well-fit, but Dunne03 estimate $L_x \sim 1 \times 10^{33}$ ergs s $^{-1}$ for this region.

Dunne03 note that the region is too young to have produced a supernova remnant and interpret the X-ray emission as hot gas filling a superbubble blown by the OB star winds, but note that the *ROSAT* X-ray luminosity for this region is three orders of magnitude lower than the predictions of standard wind-blown bubble models. They conclude that the discrepancy may be due in part to the inclusion of heat conduction across the interface between the hot X-ray emitting region and the cool swept-up shell in those models, whereas the strong magnetic field in M 17 (Brogan & Troland 2001) may suppress this heat conduction. They thus consider a bubble without heat conduction, but

can only reproduce the observations by assuming substantial mixing of cold nebular gas with the shocked stellar winds; they further require the stellar winds to be clumpy (Moffat & Robert 1994) and have reduced mass loss rates in order to get reasonable agreement between the models and their observations.

An observation with the *ASCA* satellite, which has a broad point spread function, shows emission coincident with the cluster core with 0.5–10 keV luminosity $L_x \sim 10^{33-34}$ ergs s $^{-1}$, with high plasma energy ($kT > 3$ keV, or $T > 35$ MK) and absorption ($N_H = 1$ – 5×10^{22} cm $^{-2}$) (Matsuzaki et al. 1999). These authors interpreted the emission as a point source associated with the single O4–O4 binary system, but we establish here that their spectrum is comprised of emission from many hundreds of cluster members.

On the western side, all tracers of warm and hot gas are truncated by a wall of dense, cold molecular material which includes the dense cores known as M17 Southwest and M17 North; these exhibit many other tracers of current massive star formation. These include: the Kleinmann-Wright object, an embedded $L_{bol} \simeq 2600 L_\odot$ Herbig B2e star; M17-UC1, an extremely small (diameter ~ 1000 AU) and dense ultra-compact region powered by a very young massive binary system with a luminosity of several thousand L_\odot ; the even more luminous, but radio-faint, protostar IRS 5; and a deeply embedded millimeter-infrared source (Johnson, Depree, & Goss 1998; Henning et al. 1998; Chini, Nielbock, & Beck 2000; Nielbock et al. 2001; Kassis et al. 2002). There is a strong suspicion that shocks from the blister HII region have compressed the cloud and triggered this star formation activity. The exact structural relationships between the cold and warm gaseous components are not certain; for example, neutral-hydrogen clumps may be mixed with HII gas on the edge of the molecular cloud (Clayton et al. 1985).

Only the most massive members of the young NGC 6618 stellar cluster exciting the nebula have been characterized, due to the comparatively high extinction. Near-infrared imagery and spectroscopy reveal an embedded cluster of about 100 stars earlier than B9 (Lada et al. 1991; Hanson, Howarth, & Conti 1997); see Table 5 in Appendix A for a list of O–B3 stars. These studies did not cover the entire cluster, so even more early stars may be present. This is substantially richer than the Orion Nebula Cluster which has only 8 stars between O6 and B9 (Hillenbrand 1997). Hanson, Howarth, & Conti (1997) report the age of the cluster, obtained from isochronal fitting, to be ~ 1 Myr or younger. Many of the stars in M 17 show infrared excesses attributed to disks, and a considerable fraction are close binaries (García & Mermilliod 2001). The extinction is patchy, ranging from $A_V = 3$ to 15 with an average of 8 magnitudes. From main sequence fitting of the OB stars, the distance to M 17 has been measured to be $1.3^{+0.4}_{-0.2}$ kpc (Hanson, Howarth, & Conti 1997) and 1.6 ± 0.3 kpc (Nielbock et al. 2001), significantly closer than the traditional value of $\simeq 2.2$ kpc based on the Galactic rotation curve. We adopt here a distance of 1.6 kpc.

In summary, prior to the present study, M 17 was known to have four major morphological components: (1) An inner, bright photoionized nebula with a hollow, conical shape, with gas concentrated in the northern and southern bars. The gas in the bars, photoexcited by the early OB stars, has $T_e \sim 8000$ K and $n_e \sim 10^3$ cm $^{-3}$. (2) An outer, fainter, optically thin ionized region, also with extended soft X-ray emission seen by *ROSAT*, with $T_x \sim 8$ MK and $n_e \sim 0.1$ cm $^{-3}$. This outer region lies largely outside the field of view of our *Chandra* observation.

(3) Dense, cold molecular gas surrounding the two bars with active star formation, including new rich stellar clusters. (4) The open cluster NGC 6618 which excites the nebula.

2.2. Rosette

The Rosette Nebula (= NGC 2237–2246, at $(l, b) = (206.4, -2.0)$) is powered by the open cluster NGC 2244, the youngest cluster within the larger Mon OB2 association. It is a blister HII region lying on the edge of the giant Rosette Molecular Cloud (RMC) which in turn lies within a larger H I cloud (see Pérez (1991) for a review of the large-scale star formation environment). Due to the orientation with respect to the line of sight, the extinction to the stars and nebula is lower than for M 17, generally only $A_V \sim 1\text{--}2$ mag (Celnik 1986).

The Rosette is morphologically similar to M 17 in that the nebular emission is edge-brightened, though in the case of Rosette it resembles a torus (in projection) rather than two bars. At both radio and visual wavelengths (Figures 2a and b), the Rosette HII region appears as a thick circular ring of ionized gas with an outer diameter $\sim 80'$ (~ 33 pc) and an inner hole $\sim 30'$ (~ 12 pc) in extent (Celnik 1985). The *IRAS* data show a similar annular morphology extending beyond the HII region into the photodissociation region and surrounding molecular cloud (see Figure 2c, from Cox, Deharveng, & Leene (1990)). Researchers have variously suggested that this annular or ‘hollow’ HII morphology arises from evacuation by the OB stellar winds or by the depletion of gas into newly-formed stars (Mathews 1966; Fountain, Gary, & Odell 1979; Leahy 1985; Dorland, Montmerle, & Doom 1986; McCullough 2000). The shape of the nebula is generally considered to be spherical, but it may equally well be cylindrical.

The HII region was modeled by Celnik (1985) to explain the radial distribution of brightness temperature derived from radio continuum observations. In these data, $T_e = 5800$ K and showed no radial gradient. The favored model consists of a central spherical cavity surrounded by nested spherical shells of varying density (maximum $n_e \sim 12$ cm $^{-3}$), with a conical hole penetrating the shells and oriented approximately along the line of sight. This model is further developed by Celnik (1986) into a three-dimensional model of the entire RMC and Rosette Nebula complex. In this model, the HII region is located on the near side of the molecular cloud complex; it and the molecular clouds are rotating about the center of the complex. The conical hole penetrating the shells of the HII region is oriented roughly 30° west of the line of sight, toward the nearest edge of the molecular cloud.

In a recent paper, Tsivilev et al. (2002) describe radio recombination line observations of Rosette, giving $T_e = 7980 \pm 580$ K. They build a model of the region, using a constant, average $T_e = 6400$ K and assuming that the region consists of concentric shells, similar to the Celnik (1985) model. The main new feature of the Tsivilev et al. (2002) model is the inclusion of dense clumps of material in the shells. To match the data, their model required two shells: an outer one with uniform density $n_e = 15$ cm $^{-3}$, similar to the Celnik (1985) model, and an inner one with high-density clumps ($n_e \sim 10^3\text{--}10^4$ cm $^{-3}$).

The RMC, extending a degree to the east (see Figure 2c), is a clumpy, elongated giant molecular cloud with no evidence for cloud compression or star formation close to the HII region (Williams, Blitz, & Stark 1995). The densest parts of the cloud

are populated with embedded near-infrared star clusters without massive ($L_{IR} \sim 10^3 L_\odot$) members (Phelps & Lada 1997; Schneider et al. 1998), although massive young B stars such as AFGL 961 are also seen in the *IRAS* data (Cox, Deharveng, & Leene 1990).

The NGC 2244 cluster exciting the nebula has a population intermediate between that of M 17 and the Orion Nebula Cluster, with 31 stars between O4 V and B3 V (Table 6 in Appendix A). It has a core radius of ~ 2 pc ($\sim 4.9'$), an outer radius of ~ 8 pc ($\sim 19.5'$), and low stellar density, thus it shows substantial contamination from field stars (Nilakshi et al. 2002). Curiously, the earliest exciting star (HD 46223, O4 V((f)), see Table 6) does not lie near the center of the nebula, but rather near the southeast edge of the ring. The other early-O star (HD 46150, O5 V((f))) is located near the center of the nebula. The main sequence turn-off age of the cluster is about 1.9 Myr (Park & Sung 2002), which agrees with the age inferred from the eclipsing binary V578 Mon (Hensberge, Pavlovski, & Verschueren 2000). This young age, together with the absence of nonthermal radio emission, indicates that no supernova explosion has occurred in the cluster (this point is discussed further in §6.3). The most accurate distance to NGC 2244, $d = 1.39 \pm 0.1$ kpc, is derived from modeling V578 Mon (Hensberge, Pavlovski, & Verschueren 2000). We adopt a distance of 1.4 kpc here.

As mentioned above, an *Einstein Observatory* Imaging Proportional Counter observation of NGC 2244 revealed several individual O stars and extended X-ray emission from the nebula interior, with $kT \sim 2$ keV ($T \sim 23$ MK), $n_e \sim 0.02$ cm $^{-3}$, and luminosity $L_x = 6 \times 10^{32}$ ergs s $^{-1}$ in the soft (0.5–3 keV) band (Leahy 1985). Leahy attributes this to diffuse emission from the OB winds, but the low resolution provided by this instrument could not determine the fraction of the emission from the many magnetically active lower mass pre-main sequence stars expected to accompany the massive stars. Indeed, a later higher-resolution *ROSAT* study by Berghöfer & Christian (2002) (see Figure 2d) attributed all of the emission to point sources. This *ROSAT* study (see also the closely related work of Li et al. (2002) and Park & Sung (2002)) identified 128 X-ray emitting pre-main sequence stars in addition to 10 OB stars. A separate *ROSAT* observation of the RMC revealed dozens of faint, partially resolved embedded sources attributed to individual Herbig Ae/Be stars and clusters of low-mass pre-main sequence stars (Gregorio-Hetem et al. 1998)⁵.

One aspect of the Rosette star formation region is still unclear: was the formation of the cluster triggered by an encounter between the large Monoceros Loop supernova remnant (SNR), seen in radio continuum and H α , and the RMC? The SNR may have been produced by a massive member of the Mon OB2 association; it has a diameter ~ 80 pc and is centered 2° to the northeast of the Rosette Nebula. Older studies placed it at about the same distance as NGC 2264 (~ 800 pc), but more recent estimates from a CO survey of the Mon OB1 region (Oliver, Masheder, & Thaddeus 1996) suggest that it lies at approximately the same distance as the NGC 2244 stellar cluster; note, however, that it has an estimated age of only 0.03 to 0.5 Myr (Welsh et al. 2001). Given a cluster age of 1.9 Myr (see above), the evidence suggests that the cluster formed earlier than any possible encounter with the SNR. Extended high-energy γ -ray

⁵ This study noted strong X-ray emission at the edge of the *ROSAT* PSPC field towards the HII region and speculated that it arose from either unresolved emission from T Tauri stars or from OB wind emission. It is now clear that this is emission from the unresolved O4 V star HD 46223 blurred by the poor point spread function at that off-axis location in the *ROSAT* image.

emission has been found by the EGRET instrument around the region of apparent contact between the SNR and the nebula, interpreted in terms of π° decay resulting from collisions between SNR-accelerated particles and the molecular cloud (Jaffe et al. 1997). However, no morphological indication of a collision or compression is evident from optical or molecular maps.

In summary, and by analogy with M 17, the major morphological components of the Rosette star formation region are: (1) An edge-brightened, photoionized nebula with a hollow, spherical (or cylindrical) shape, perhaps with a conical cavity expanding towards the nearest edge of the surrounding molecular cloud. The central region showed extended X-ray emission with *Einstein*, with $T_x \sim 23$ MK and $n_e \sim 0.02$ cm $^{-3}$, but *ROSAT* studies resolved this emission into point sources. Shells of higher density surround the hollow core, with $T_e \sim 6400$ K, perhaps a clumpy inner shell with $n_e \sim 10^3$ – 10^4 cm $^{-3}$, and an outer shell or shells with $n_e \sim 10$ cm $^{-3}$ (Celnik 1985; Tsivilev et al. 2002). (2) A photodissociation region between the Rosette blister HII region and its molecular cloud. (3) Dense, cold molecular gas making up the Rosette Molecular Cloud and extending far beyond the HII region, where new stellar clusters are forming. (4) The open cluster NGC 2244 which excites the nebula.

3. *chandra* OBSERVATIONS AND ANALYSIS

The HII regions were observed with the Imaging Array of *Chandra*'s Advanced CCD Imaging Spectrometer (ACIS-I); the observatory and instrument are described by Weisskopf et al. (2002). CCDs S2 and S3 from the Spectroscopy Array were also operating, although these chips are $> 15'$ off-axis and not positioned to match the ACIS-I focal surface, so they exhibit large, distorted PSFs that make point source detection difficult. They are nonetheless useful for broad characterization of diffuse emission and for revealing the presence of bright point sources. The observing mode was the standard ‘‘Timed Event, Faint’’ mode, with 3.2-sec integration times, 0.041-sec frame readout times, and 3×3 pixel event islands.

Table 1 gives the observing log. M 17 was observed in a single 39 ks pointing centered on the heavily obscured O4–O4 binary known as Kleinmann’s Anonymous Star in the NGC 6618 cluster (star #1 in Chini, Elsaesser, & Neckel (1980); #341 in Ogura & Ishida (1981); #189 in Hanson, Howarth, & Conti (1997)). The Rosette observation consisted of a contiguous sequence of four ~ 20 -ks ACIS-I snapshots (Fields 1–4), resulting in a $\sim 1^{\circ} \times 0.25^{\circ}$ mosaic of the Rosette Nebula and Rosette Molecular Cloud (RMC). The aimpoint of Rosette Field 1 was placed near the center of the Rosette Nebula on the B star HD 259105, to avoid photon pile-up of the O5 star HD 46150. An unfortunate telescope roll angle about this aimpoint led to HD 46150 falling in the gap between CCDs I2 and I3, resulting in substantially reduced exposure for this important early O star. Rosette Field 2 yields the best image of the interface between ionized material in the HII region and neutral material in the RMC. Fields 3 and 4 step eastward into the molecular cloud, sampling the young, embedded stellar population there.

Our custom processing, starting with the Level 1 data stream, is described in Appendix B. Important steps include removal of the $0.5''$ position randomization and correction of the CCD charge transfer inefficiency (CTI) to improve spectral resolution (Townesley et al. 2002a). We generated custom response matrix

files (RMFs) and quantum efficiency uniformity files (QEU) to facilitate spectral fitting of CTI-corrected data (Townesley et al. 2002b)⁶. The images are registered with the USNO A2.0 catalog (Monet et al. 1998) or Hipparcos sources (Høg et al. 2000) in the field to improve the astrometry; this alignment is accurate to about $\pm 0.3''$.

To search for and quantify any diffuse emission in the regions, we have performed a variety of smoothing and image processing steps; results are shown in Figures 3 through 5 for M 17 and Figures 6 and 7 for Rosette. For display purposes, the photon counting images are smoothed with an adaptive kernel filter using the *csmooth* program (a translation of the *asmooth* code by Harald Ebeling), part of the CIAO data analysis system supplied by the *Chandra* X-ray Center (CXC). The ACIS-I exposure maps, which take into account a variety of effects (e.g., bad CCD columns, gaps between the CCDs, telescope vignetting, and satellite dithering), are similarly smoothed and the resulting photon and exposure images are divided to give a view of the X-ray flux distribution with all known instrumental effects removed.

Figures 3a and 6a show the ACIS-I flux images at this stage of the data processing. The images here are shown at reduced resolution after adaptive kernel smoothing with *csmooth*. In these two-color images, red intensity is scaled to the soft (0.5–2 keV) brightness and blue intensity is scaled to the hard (2–8 keV) brightness. For clarity, the soft and hard smoothed images are shown separately in Figures 3b and c and 6b and c. Both fields show clear indications of soft extended emission in addition to hundreds of unresolved sources.

Quantitative study of the extended emission requires removal of the point source events. Point sources were found using the wavelet-based source detection program *wavdetect* (Freeman et al. 2002). After experimentation with the source significance threshold in *wavdetect*, we chose a threshold level $P = 1 \times 10^{-5}$. While this results in a number of faint (3–5 counts) and possibly spurious sources, it is more sensitive to clearly real sources that are missed (especially when there is underlying diffuse emission) at the usual threshold of $P = 1 \times 10^{-6}$. The fields were carefully examined by eye to identify potential point sources missed by *wavdetect* due to crowding, diffuse emission, or unknown reasons. The resulting lists of point sources and identifications with members of the NGC 6618, NGC 2244, and RMC stellar clusters will be discussed in separate studies.

Once this liberal list of potential point sources was established for each field, we used our custom IDL code *acis_extract* to excise them from the data⁷. This tool uses the point spread function (PSF) library in the CIAO Calibration Database to generate a polygon around each source that represents the 99% contour of the PSF at a chosen energy (typically 1.5 keV). A circular exclusion zone is generated with diameter 1.1 times larger than the largest polygon cord. All events within these exclusion zones are deleted, resulting in the ‘sources-removed’ (or, more informally, ‘swiss-cheese’) event list. The full-band swiss-cheese images for the M 17 and Rosette data are shown at reduced resolution (8-pixel binning) in Figures 4a and 7a, respectively.

4. MORPHOLOGY OF THE DIFFUSE X-RAY EMISSION

4.1. M 17

⁶ Details, source code, and calibration products for CTI correction using our method are available at <http://www.astro.psu.edu/users/townesley/cti>.

⁷ The *acis_extract* code is available at http://www.astro.psu.edu/xray/docs/TARA/ae_users_guide.html.

Figure 4b shows the $17' \times 17'$ ACIS image of the densest parts of M 17, with the ~ 900 sources removed by the ‘swiss-cheese’ procedure explained above, smoothed with our own adaptive smoothing algorithm. This algorithm understands the absence of data (the holes where point sources were) and does not introduce edge effects into the smoothed image; see Appendix C for details. Red areas highlight soft (0.5–2 keV) emission and blue areas highlight hard (2–7 keV) emission⁸. The holes from the masked point sources are shown at their full size in panel b, to give a smoothed representation of the data that still retains much of the character of the simple binned image (panel a). Panel c shows these holes partially smoothed over; in panel d they are completely smoothed over. These three versions of the adaptively-smoothed unresolved emission in M 17 are shown to provide the reader with an incremental transition from the swiss-cheese image to the fully-smoothed image; the intent is to illustrate that, although smoothing can reveal morphological features impossible to see in the binned data, it can cause the viewer to lose track of the actual amount of information that went into the smoothed image. These smoothed images are reassuringly similar to the *csmooth* image in Figure 3a.

Figure 5 explores the soft diffuse emission in more detail. Panel a shows a three-color image of the soft emission with the point source masks in place; here red = 600–700 eV, green = 830–940 eV, and blue = 1280–1540 eV. The spectrum in panel b uses 20-eV bins to show the line features that motivated the bands selected for panel a. The three-color image allows us to scale the brightness of the 600–700 eV component up to show faint soft features; a slight enhancement to the northwest of the core of NGC 6618 is visible in this image. This image hints at a possible softening of the X-rays with distance away from the ionizing cluster; although our spectral analysis to search for changes in the temperature of the gas as a function of distance from the ionizing cluster showed no such evolution (see §5.2), the wider region sampled by *ROSAT* shows a slight spectral softening to the north, consistent with Figure 5a (Dunne03).

The smoothed images in Figures 3 and 4 are clearly closely related to the 2MASS near-infrared image (Figure 1c): the bright soft X-ray contours closely follow the hollow structure of the photoionized region between the northern and southern bars (while fainter emission is spread over a larger area). The brightest soft X-ray emission coincides with the hole in the diffuse HII emission in the deep near-infrared image of Ando et al. (2002) immediately around the exciting stars of the nebula. The hard emission coincides with the central region and crosses the dark region to the west of the steep interface between the photoionized bars and the molecular cloud. Another patch of hard emission is associated with the deeply embedded M 17 North region. As discussed below, the most likely source of this very slight excess of hard photons is the unresolved point source population in these embedded star-forming regions. The smoothing algorithm enhances the appearance of this emission but its proximity to regions of large point source concentrations makes this the simplest explanation.

The overall morphology of the soft diffuse emission in the ACIS image of M 17 strongly suggests that the hot gas originates in the OB cluster and flows outwards towards the lower density regions to the east. This might be called an ‘X-ray fountain,’ representing the flow of shocked OB winds into the hot

interstellar medium. The *ROSAT* PSPC image confirms this view: in the optically thick inner HII region, its contours are elongated identically to the ACIS emission while in the outer regions, it reveals the X-ray flow extending several parsecs to the east and north; this is illustrated clearly in Dunne03 (their Figure 1). Since 10^4 K HII region gas and 10^7 K X-ray gas cannot stably coexist in the same volume, it is likely that the X-ray gas fills the interior of the cylindrical or conical inner region defined by the radio/optical HII bars.

Farther to the east, the X-ray gas expands into the lower-density, optically thin region, filling a cavity in the DSS image. We suspect that the X-ray filled cavity extends farther to the north and east as traced by 330 MHz radio emission, but is obscured in both soft X-rays and H α by intervening cloud material. The X-ray emitting area may thus be 2–3 times larger than seen with *ROSAT*, and several times larger than seen in our single $17' \times 17'$ *Chandra* pointing.

In summary, the soft X-ray images of M 17 from *ROSAT* and *Chandra*, combined with radio, optical, and NIR data, strongly suggest a dynamic rather than static hot plasma, generated at the OB star cluster and flowing into (and perhaps even creating) the low-density, blister-like cavity extending 5–10 pc away from the molecular cloud. It is then unclear whether the features in the H α maps—wisps, arcs, and filaments—are manifestations of OB photoionization or direct thermal contact with the hot, X-ray emitting gas.

4.2. Rosette

Figure 7b shows the full ACIS image of the Rosette Nebula, with the ~ 350 sources removed by the ‘swiss-cheese’ procedure explained above and again smoothed with our own adaptive smoothing algorithm (see Appendix C). Red areas highlight soft (0.5–2 keV) emission and blue areas highlight hard (2–7 keV) emission. The holes from the masked point sources are shown at their full size in panel b; panel c shows these holes partially smoothed over and in panel d they are completely smoothed over. Again, these images are similar to the *csmooth* versions in Figure 6. The brightest areas of diffuse emission are coincident with the two early O stars in the field; this is not obvious in the adaptively smoothed images because they have been scaled to highlight faint diffuse emission. The ‘hot spot’ to the southwest of the main region of diffuse emission in Figures 7b–d may be due to a point source that was too faint to be detected so far off-axis.

The adaptively-smoothed images in Figure 7b–d retain the off-axis CCDs S2 (upper left) and S3 (upper right). S3 is a backside-illuminated CCD and shows higher background, thus the apparent high intensity of soft emission is dominated by detector effects and little useful information on the true soft diffuse emission is available from this device. The S2 chip may be affected by unresolved point source emission, although the diffuse emission seen in the smoothed images could be real; its spectrum is similar to the soft diffuse emission seen on the ACIS-I CCDs in this pointing.

The diffuse emission found in our *Chandra* mosaic of the Rosette region comes mainly from Field 1, which includes the NGC 2244 exciting cluster, and to a lesser extent from the northwest part of the adjacent Field 2 (see Figure 6b). Diffuse emission may very well extend outside of our ACIS fields. The total number of diffuse photons in our ACIS images of Rosette

⁸ For all smoothed swiss-cheese images of diffuse emission, we clipped the hard band at 7 keV to avoid contamination from the faint instrumental Ni K α line at 7.47 keV.

is three times smaller than in our M 17 image, thus the spectral and morphological information is limited. A longer *Chandra* exposure of Field 1 is approved for more detailed study.

With these limitations in mind, the morphology of the Rosette diffuse X-ray emission shown in the adaptively-smoothed images in Figure 6 and 7 is similar to that in M 17. It appears centrally brightened, centered to the southeast of the axis of the ionized HII torus toward the two earliest stars of the exciting cluster, HD 46223 and HD 46150 (see Table 6 in Appendix A). The surface brightness is highest around these two early O stars and decreases outwards, with possible leakage beyond the edge of the ionized shell towards the southeast, where there is a suggestion of a cavity in the optical HII region (Figure 2b). In light of the M 17 morphology described in §4.1, we can speculate that the Rosette Nebula diffuse emission might also be an ‘X-ray fountain’ generated by the exciting cluster NGC 2244 but seen almost along, rather than perpendicular to, the outflow axis, perhaps flowing out the conical cavity proposed by Celnik (1986). The fact that the Rosette diffuse emission is substantially weaker than that in M 17 is consistent with production by OB stellar winds, which are fewer and weaker in Rosette (compare Tables 5 and 6).

5. QUANTITATIVE STUDY OF THE EXTENDED EMISSION

5.1. Spectral Analysis Methodology

The ACIS detector gives moderate-resolution X-ray spectra for each of roughly 100,000 independent spatially resolved locations across its $17' \times 17'$ field of view. Having spatially decomposed the images into pixels containing point source photons and pixels containing diffuse source photons (§3), we can readily construct composite spectra for these components. For M 17, we selected the part of the ACIS-I image that contained the brightest diffuse emission (called “Total Diffuse Region” in Figure 8a) and extracted the diffuse-emission spectrum from only that region; for Rosette, we extracted counts from the entire ACIS-I array to form the diffuse-emission spectrum. For both fields, composite point source spectra were extracted by using all the point sources in the ACIS-I array.

The background contribution should be small for the point source components, since the source events were extracted from regions tailored to contain only the inner 90% of each source’s PSF. Background removal for the faint diffuse components, however, must be performed carefully. For the Rosette diffuse emission fit, we subtracted a background spectrum obtained from the S2 chip, which lay outside the core of the cluster⁹. This background spectrum was scaled by the effective area (BACKSCAL was converted to an energy-dependent vector) and by the ratio of the geometric areas. Further scaling was done to account for the non-uniform spatial distribution of the particle background¹⁰, obtained by matching the strength of the instrumental Ni K α line and the 3–7 keV continuum level. The prominent Au M line complex (around 2.1 keV) remaining in the spectrum after background subtraction (see Table 3 in Townsley et al. 2002b) may indicate that the spatial distribution of Au M fluorescent photons (which come from bombardment of gold-coated surfaces of the ACIS camera and the telescope

by solar energetic particles) does not follow that of the particle background.

Accounting for differences in geometric area, ancillary response files (ARFs), and particle background as described above, and assuming that all emission on S2 is due to background and not unresolved stars or diffuse emission, we estimate that the background accounts for about 58% of the events in our sample of the Rosette diffuse emission. Subtracting this leaves only 3300 source counts distributed over the entire ACIS-I array. Figure 7b–d implies, however, that some of the S2 photons are not from the background; if this is the case then our background subtraction removes legitimate photons from the Rosette diffuse emission spectrum and a smaller percentage of unresolved events come from the background.

For M 17, a background region near the southern edge of the I-array around the molecular cloud was used. This background spectrum was also scaled by the effective area and by the ratio of the geometric areas. Scaling the number of 0.5–2.3 keV counts in the M 17 background area (lower part of I1 chip) to account for the difference in geometric area between the diffuse-emission region and the background region, and ignoring any additional scaling due to ARF differences (the exposure map shows that this is a small factor), we find that the background accounts for almost 50% of the events in the diffuse region. This presumes that the region we used for background is free of diffuse emission, but the *ROSAT* image shows that there is faint diffuse emission in this region. The spectrum of this region also resembles that of the diffuse emission. This shows that again our background subtraction is almost certainly removing useful diffuse photons and the actual background contribution to the diffuse emission is likely less than 50%.

For both Rosette and M 17, the regions used to sample the background spectrum are not ideal. We chose not to use generic background files supplied by the CXC because our fields are in the Galactic plane, which is known to contain diffuse X-ray emission from a variety of known (e.g., the Local Hot Bubble, Snowden et al. (1998)) and unknown (e.g., the Galactic Ridge X-ray Emission, Ebisawa et al. (2001)) sources. Other nearby regions (Fields 2–4 in the Rosette observation and the western side of the M 17 observation, which includes the S2 and S3 chips) sample more obscured parts of the molecular clouds, so backgrounds generated from these regions would not be representative of the regions used to sample the diffuse emission. So rather than choosing background regions that were clearly incorrect, we decided to sample more representative regions and suffer the loss of useful photons.

The background-subtracted diffuse emission spectra, the composite point source spectra, and their associated best-fit plasma models are shown in Figure 9, with details given in Table 2. The spectral fits were performed with XSPEC (Arnaud 1996) using both the *mekal* and *vmekal* thermal plasma models (Mewe, Lemen, & van den Oord 1986; Kaastra 1992; Liedahl, Osterheld, & Goldstein 1995) and the *apec* and *vapec* models (Smith et al. 2001), where the “v” designation provides for non-solar abundances of the elements. The fits from both types of models were similar, so only the *apec* class of models is pre-

⁹ We chose to form the Rosette Field 1 background from the off-axis S2 data, rather than using the I-array data from one of the other Rosette fields, because there was a background flare during the Field 1 observation. This flare was of modest brightness but lasted for 30% of the 20-ks observation. The hard (2–8 keV) band emission varied erratically up to a factor of 3 higher than the usual background level. The variations were much less evident in the soft (0.5–2 keV) band, rising < 50% in the 1–2 keV range and negligibly below 1 keV. Since flares clearly affect the spectral shape of the background, we determined that better background subtraction could be achieved by using the off-axis S2 data (with appropriate scaling) rather than a different observation. Our composite point source spectral analysis for Rosette Field 1 was restricted to the 0.7–5 keV band to minimize the effect of these background variations.

¹⁰ Catherine Grant, private comm.; also see <http://space.mit.edu/~cgrant/cti/cti120.html>.

sented here. One or two absorption components were included via the *wabs* model (Morrison & McCammon 1983). An additional absorption component, due presumably to hydrocarbon deposition on the ACIS optical blocking filters (Chartas et al. 2002), was also included in the XSPEC model¹¹. The spectral fits employed count-weighted ARFs made using the CIAO utility *mkwarf*. We chose to use the single CTI-corrected response matrix file (RMF) (Townsend et al. 2002b) that coincided with the largest fraction of counts. For the full-field spectral fits shown in Figure 9, the RMFs used were the full-CCD versions, so the spectral resolution is the average across the entire CCD after CTI correction (see Appendix B). These full-CCD CTI-corrected RMFs are similar to each other, so using a single-CCD RMF for the entire I-array does not introduce substantial errors.

Table 2 shows that the background-subtracted diffuse emission in both HII regions is reasonably well-represented by a two-temperature thermal plasma with a single absorbing column. The temperatures of both plasma components are comparable between the two regions. The Gaussian at ~ 2.1 keV was included to model the instrumental Au M complex discussed above. For both regions, the kT_1 component was fixed to solar abundances while the kT_2 component was a variable-abundance plasma.

For comparison with the diffuse emission, we performed similar spectral fits on the emission from the combined point sources detected in the HII regions. Again the kT_1 component was fixed to solar abundances while the abundances for the kT_2 component were allowed to vary. The Rosette composite point source spectrum was adequately fit by plasmas at 0.2 and 2.1 keV with a single absorbing column. Fitting the combined M 17 point sources required a more complicated model: a solar-abundance thermal plasma at 0.19 keV with a relatively low absorption ($7 \times 10^{21} \text{ cm}^{-2}$) and a variable-abundance thermal plasma (3 keV) with higher absorption ($17 \times 10^{21} \text{ cm}^{-2}$). This fit was also clearly improved by adding Gaussians at 1.1, 1.3, and 6.7 keV; lines at these energies are seen in O stars and in flaring pre-main sequence stars (e.g., Schulz et al. 2000; Tsuboi et al. 1998). No line was needed to model the instrumental Au M complex in the combined point source spectra, indicating that no significant residual instrumental background is present around 2 keV.

In addition to the introduction of Gaussian lines, we found that extra-solar abundances of oxygen were needed to give a good fit to all of the spectra, and extra-solar abundances of neon were needed for the point source spectra, although the actual abundance values were not well-constrained. If both plasma components are forced to have solar abundances in the M 17 spectra, the fits are statistically worse. The reduced χ^2 for the diffuse spectrum increases from 1.2 to 1.4; the plasma temperatures did not change but N_H increased from $4 \times 10^{21} \text{ cm}^{-2}$ to $6 \times 10^{21} \text{ cm}^{-2}$. For the composite point source spectrum, the reduced χ^2 went from 1.5 to 3.7; the two absorption values and the first plasma component's temperature stayed the same, but the second plasma component increased from $kT_2 = 3.0$ keV to $kT_2 = 3.6$ keV. This caused the iron line to be too strong (even with elimination of the Gaussian at 6.7 keV) and was the major reason for the unacceptable fit.

Similar results were obtained for Rosette. Requiring both plasma components to have solar abundances in the fit to the

diffuse spectrum caused the reduced χ^2 to increase from 0.7 to 1.3. As for M 17, the plasma temperatures did not change but N_H increased, here from $2 \times 10^{21} \text{ cm}^{-2}$ to $5 \times 10^{21} \text{ cm}^{-2}$. For the composite point source spectrum, the reduced χ^2 went from 1.6 to 3.0; the absorption stayed the same, but both plasma components increased in temperature: kT_1 went from 0.20 to 0.29 keV and kT_2 went from 2.1 to 2.9 keV. This caused large residuals below 2 keV—the model appeared to have many more line-like peaks than the data.

There are several reasons why including non-solar abundances might improve the fit to these composite spectra. Excess NeIX and NeX lines are prominent in the spectra of nearby flaring late-type stars (Brinkman et al. 2001) and can be present in pre-main sequence flaring stars as well. The origin of excess oxygen is less clear. We suspect that it is not astrophysically real, but arises from inadequate modeling of the absorption. Each spectrum covers stars or regions with a wide range of foreground absorptions, leading to a confused observed spectrum in the < 1 keV region, where oxygen has strong lines. The Gaussians needed to fit the M 17 composite point source spectrum and other features seen in the (Data–Model) residuals in Figure 9 may also arise from the merging of different plasma conditions into a single spectrum. Imperfect background removal accounts for the residuals at low and high energies.

5.2. Spectral Results

The resulting plasma spectra are shown in Figure 9 and the parameters of the best-fit plasma models are given in Table 2. L_{soft} values are the soft-band (0.5–2 keV) X-ray luminosities assuming distances of 1.6 kpc for M 17 and 1.4 kpc for the Rosette Nebula; absorption-corrected values are given as L_{soft}^c . There is substantial hard-band (2–7 keV) flux only for the M 17 combined point sources, where the absorption-corrected luminosity is $L_{\text{hard}}^c \simeq 4.1 \times 10^{33} \text{ ergs s}^{-1}$. The temperatures of both diffuse-emission plasma components are very similar in the two regions and are dominated by the $T \sim 10$ MK component, with a secondary 1 MK component. But the regions are notably different in luminosity and surface brightness, with the M 17 diffuse emission a factor of > 5 brighter than the Rosette diffuse emission and coming from an extraction area $\sim 90\%$ as big as that used to sample the Rosette diffuse emission (roughly 42 pc^2 vs. 47 pc^2). Equivalently, we see that the diffuse component comprises $\simeq 36\%$ of the total soft luminosity in the M 17 region sampled but only $\simeq 7\%$ in the Rosette Nebula region.

To within the errors, our kT_2 plasma component is consistent with the Dunne03 results from spectral modeling of the *ROSAT* data on M 17. This is somewhat remarkable, since the *Chandra* data have shown that point sources contribute substantially to the X-ray emission in the *ROSAT* band. Our value for N_H is substantially larger than the Dunne03 value for their Regions A and C but is consistent with their N_H for Region D. The large section of the ACIS field that was used to sample the diffuse emission encompasses most of Dunne03 Regions C and D and part of their Region A, but it also extends farther to the north and west than those regions, into parts of the nebula that are more highly absorbed. This may account for our higher N_H estimate.

No hard diffuse component was detected in either ACIS field, when all diffuse counts were combined into a single spectrum. The smoothed X-ray images in Figures 3c and 4b–d suggest that

¹¹ This instrumental issue is discussed at http://cxc.harvard.edu/cal/Acis/Cal_prods/qeDeg/index.html. The correction program and XSPEC model *acisabs* was developed by George Chartas and is available at <http://www.astro.psu.edu/users/chartas/xcontdir/xcont.html>.

a diffuse hard component might be present in M 17, towards the M 17SW molecular cloud and M 17 North protostellar region. However, this emission is spatially coincident with high concentrations of point sources and, once those point sources are removed from the data, few hard counts are left to contribute to the global diffuse spectrum (see the swiss-cheese image, Figure 4a).

There are enough diffuse counts in M 17 to warrant subdividing them into smaller regions to search for spatial gradients in temperature. Two such schemes are shown in Figure 8, one sensitive to temperature effects associated with proximity to the molecular boundaries of the HII region cavity, and the other sensitive to cooling as the gas flows eastward from the central O stars. In almost all cases, no changes in plasma components were found. The only discrepant case is the westernmost box in (b) which showed 2.3 and 23 MK (0.2 and 2 keV) components (plus stronger absorption, with $N_H = 14 \times 10^{21} \text{ cm}^{-2}$). These properties may reflect either a change in plasma conditions or contamination by an unresolved population of lower-mass stars (see §6.2).

Finally, we note that the composite spectra of the point sources are complex in different ways (Figure 9). Even complicated spectral models do not give statistically acceptable fits. This is understandable given that we have combined hundreds of different stars, each of which suffers different absorption and may have spatially and temporally variable plasma emission, to generate these composite spectra. The presence of excess neon and the iron line at 6.7 keV supports the interpretation that these are magnetically active flaring stellar sources. A soft ($kT \sim 0.2 \text{ keV}$) spectral component is seen in the composite point source spectra of both M 17 and Rosette; this may be simply a component of the stellar plasma, although Wolk et al. (2002) see a similar soft component in extended emission in RCW 38 and note that it may be partially caused by X-ray halos around the point sources, due to dust scattering. In any case, we have no evidence that the physical mechanism generating this soft plasma component in the stellar spectra is related to the soft component seen in the diffuse emission. The most important result for our purposes here is that in both star-forming regions the point sources are dominated by a substantially harder plasma component (2–3 keV, or 23–35 MK) than seen in the diffuse emission ($\sim 0.7 \text{ keV}$, or 8 MK).

5.3. Physical Properties of the Plasma

It is clear from the above analysis that the diffuse X-ray emission in both the Rosette Nebula and M 17 is due predominantly to a hot plasma. The physical parameters can readily be estimated, with results summarized in Table 3.

For both nebulae, our *Chandra* results show relaxed center-filled morphologies (§4). M 17 lacks any measurable temperature gradients (§5), although Figure 5 hints that such gradients may be present; too few diffuse counts are present in our Rosette observation to search for such gradients. We therefore consider the simple situation of a uniform, optically thin, isothermal plasma in a simple geometry. For simplicity, we will assume that the diffuse X-ray luminosities given in Table 2 come from the idealized emitting regions defined below; in reality of course the emission has a more complex structure.

For M 17, we adopt a cylindrical geometry viewed perpendicular to its axis with radius $3.5'$ ($r = 1.6 \text{ pc}$) and length $8'$ ($l = 3.7 \text{ pc}$), giving a plasma volume $V_x = \pi r^2 l = 9 \times 10^{56} \text{ cm}^3$. For the plasma volume V_x in Rosette, the emitting region can be ap-

proximated by a circle of radius $4.7'$ ($r = 1.9 \text{ pc}$) and we adopt a spherical geometry with volume $V_x = \frac{4}{3}\pi r^3 = 9 \times 10^{56} \text{ cm}^3$. We introduce a geometric correction factor η of order unity to account for the possibility that the emitting regions are flattened or elongated along the line of sight. This is simultaneously used as a filling factor ($\eta < 1$) if the plasma density is inhomogeneous due to shocks or the penetration of cooler gas. We thus retain η as a free scaling parameter of the inferred physical parameters of the X-ray gas, but find that most quantities depend only weakly on η . Recall that the true X-ray luminosity and emitting volume is undoubtedly larger than used here (probably by a factor > 2 for M 17 and < 2 for Rosette), as we restrict our diffuse photon extraction to regions with high surface brightness.

The plasma luminosities $L_{x,bol} = \beta L_x$ considered here scale the absorption-corrected X-ray luminosities given in Table 2 by a bolometric correction factor $\beta \simeq 1.3$ for $kT = 0.6\text{--}0.8 \text{ keV}$ to account for emission lying outside of the Chandra spectral band. Although the best fit spectra are multitemperature, for simplicity we consider here the plasmas to be isothermal at the dominant energy around $kT = 0.7 \text{ keV}$.

From the three measured quantities $L_{x,bol}$, V_x , and T_x , the basic physical parameters of the plasma can be derived. The plasma electron density $n_{e,x}$ is obtained from $L_{x,bol} = \Lambda n_{e,x}^2 \eta V_x \text{ ergs s}^{-1}$, where $\Lambda = 5 \times 10^{-23} \text{ ergs cm}^3 \text{ s}^{-1}$ is the bolometric X-ray emissivity for a cosmic abundance plasma at $kT_x = 0.7 \text{ keV}$ based on the CHIANTI emission line database (Landi & Landini 1999). Λ is only weakly dependent on temperature close to $kT_x \approx 1 \text{ keV}$. For a fully ionized cosmic abundance plasma, the mean molecular weight per electron is $\mu_x = 0.62$. Knowing $n_{e,x}$ and T_x , the plasma pressure is then $P_x/k = \rho T_x / (\mu_x m_p) = 2.2 n_{e,x} T_x$, the thermal energy $E_x = \frac{3}{2} P_x V_x$, and the cooling timescale $\tau_{cool} = E_x / L_{x,bol}$. The total mass of the X-ray gas is $M_x = \mu_x m_p n_{e,x} V_x$. The timescale for dynamical equilibration across the X-ray regions is $\tau_{equil} = r / v_s \simeq 1 \times 10^4 \text{ yr}$ where $v_s = 0.1 T_x^{1/2} \text{ km s}^{-1}$ is the plasma sound speed. This short equilibration timescale indicates that the X-ray plasma should quickly fill most of the HII region volume, supporting the assumption of a constant temperature over the X-ray emitting region except where shocks are present. The X-ray morphologies of both regions are center-filled and roughly consistent with the uniform plasma assumed here, although deeper exposures may reveal inhomogeneities due to shocks.

In addition to providing these quantities for the M 17 and Rosette X-ray emitting regions in Table 3, we compare them with properties of the HII photodissociation regions that surround the X-ray gas based on published radio and optical studies. Note that at these lower temperatures helium is only partially ionized: Celnik (1985) gives $N(\text{He}^+)/N(\text{H}^+) = 0.12$ for the Rosette. Then the mean molecular weight per electron in the photodissociation region is $\mu_{II} = 0.95$, and $P_{II}/k = 1.4 n_{e,II} T_{II}$. We also assume $\eta = 1$ for this HII gas, which may not be correct if the warm gas is filamentary as suggested by recent high-resolution optical and infrared images (Jiang et al. 2002). We use the values of T_{II} and $n_{e,II}$ given in Tsvilev et al. (2002) for Rosette.

We can first compare the gas pressures of the X-ray and HII regions. In M 17, the X-ray plasma and photodissociation region pressures are approximately equal, so that the plasma probably does not expand radially, perpendicular to the axis of the HII cylinder. Unfortunately, the HII pressure in the low-density side east of this cylinder is unmeasured, but it is possible that the X-ray plasma is unconfined and expands in that

direction. The similarity between the radio, optical, and *ROSAT* images (Figure 1) would however suggest that it is at least partially confined. We can compare our estimate of T_x and $n_{e,x}$ to the *ROSAT* results for M 17: Dunne03 find $T_x = 8.5 \times 10^6$ K and $n_{e,x} = 0.09 \text{ cm}^{-3}$. The X-ray temperatures are comparable to within the errors but the density is somewhat lower; this is expected because the *ROSAT* data sample the fainter, more extended emission eastward of the ionizing cluster that is missed in the smaller ACIS-I field of view.

Rosette is similar: the nominal pressure of the X-ray plasma is the same as the photodissociation region pressure, if we assume that the model of Tsivilev et al. (2002) is correct and the inner shell contains high-density clumps ($n_{e,II} = 10^3 \text{ cm}^{-3}$). However, there is still a difficulty in explaining why the Rosette cavity is much smaller than it should be according to standard bubble models (§7). There are two possible explanations here: either the plasma volume is greatly elongated along the line of sight so that $\eta \gg 1$ and the density is considerably lower than we estimate here, or the plasma escapes and flows into the surrounding interstellar medium. As mentioned above, this flow might be an unimpeded ‘X-ray fountain’ roughly along the line of sight, as we clearly see in M 17 nearly in the plane of the sky, and/or a leakage of X-ray gas through fissures in the HII and molecular gas.

6. POSSIBLE ORIGINS OF THE EXTENDED EMISSION

6.1. Instrumental Effects

We are quite confident that the extended emission does not arise from some instrumental effect. For each source, the *acis_extract* procedure (§3) calculates the polygon enclosing 99% of the PSF, then masks out a circular region 1.1 times larger than the largest cord of this polygon to create the swiss-cheese image. Thus we have been very careful to remove all of the emission from detected point sources, accounting for the size and shape of the point spread function at different locations on the detector. Residual contamination from known point sources should therefore contribute negligibly to the measured diffuse emission (Table 2).

There are no known spatial variations in the background events in the ACIS-I array which mimic either the M 17 or Rosette diffuse emission. As discussed in §5.1, a temporal flare occurred during the Rosette observation but had little effect on the soft band where the diffuse emission appears; flare events also should be distributed roughly uniformly across the detector.

6.2. Low Mass Pre-Main Sequence Stars

There is a more serious concern that a large number of cluster members which are too faint to be individually detected as point sources may mimic diffuse emission. This indeed was a significant problem with the earlier *Einstein* and *ROSAT* studies of high-mass star formation regions (§1). We can quantitatively evaluate this effect by comparing the M 17 and Rosette clusters to the Orion Nebula Cluster (ONC) and its environs, for which there is both a more complete stellar census and deeper *Chandra* X-ray coverage than for the clusters considered here (Feigelson et al. 2002, see their Tables 2, 3, and 5). We assume here that the ONC, M 17, and Rosette stellar clusters have identical IMFs with identical X-ray luminosity functions, differing only in their total population. Since M 17 (Rosette) has 51 (up to 31) members with spectral type B3 or earlier (if we assume that most stars listed in Table 6 are members of NGC 2244)

compared to 8 high mass stars in the ONC, we infer that they have ~ 6 (~ 4) times the low mass population of the ONC. The ONC has 1075 *Chandra* detections above 0.10 cts ks^{-1} in the ACIS-I detector. Our sensitivity to point sources in the M 17 (Rosette) fields, scaling by both exposure time and distance, is equivalent to sensitivities of 2.7 (4.0) cts ks^{-1} in the ONC. Examining the ONC source count distribution and scaling upward by a factor of 6 (4) to match the overall cluster populations, we predict the detection of 1960 sources in M 17 and 900 sources in Rosette. This is about a factor of 2 higher than the number of sources detected in M 17 and in Rosette Field 1. However, since many of the ONC sources are from an embedded population behind the HII region, while in M 17 and Rosette these embedded stars are mainly displaced from the HII region, we believe this difference is not significant.

Having established that the detected ONC, M 17, and Rosette source counts are at least roughly compatible, we now use the deeper ONC observation to obtain the coarse estimate that 4500 (6100) undetected sources emitting 3×10^{32} (5×10^{32}) ergs s^{-1} should be present in the M 17 (Rosette) fields (more Rosette sources remain undetected mainly because our observation of Rosette Field 1 is half as long as our M 17 observation). This is about 8% (80%) of the absorption-corrected diffuse X-ray luminosity L_{soft}^c shown in Table 2. For M 17, this result clearly supports the already convincing morphological evidence that very little of the ‘diffuse’ emission can arise from the undetected population of X-ray-faint cluster members. The situation is not quite so clear for Rosette, where our calculation permits that a significant fraction, even most, of the ‘diffuse’ emission could come from undetected stars—note that this calculation is very rough, though, and could easily be in error by a factor of 2. The difference in spectral shape between the ‘diffuse’ and the detected point source components (compare panels b and d in Figure 9), however, independently indicates that the point source contribution to the diffuse emission is small. The issue will be easily settled with the upcoming deeper *Chandra* observation of Rosette: from the ONC source count distribution, we estimate that a 100 ks exposure should resolve about half of the emission from stars that are currently undetected.

6.3. Supernova Remnants

In M 17, there are many arguments against a hypothesis that the X-rays are independent of the HII gas and instead arise from the remnant of a recent supernova explosion. Foremost, the X-ray morphology follows very closely the morphology of the thermal radio and optical emitting HII region (§4.1) which does not show kinematic disturbances greater than $\simeq 100 \text{ km s}^{-1}$. In addition, the stellar cluster currently has no stars evolved off of the main sequence, indicating a young age, and is insufficiently rich to host a population of extremely massive stars which could evolve extremely rapidly into a supernova. Even in a cluster with 100 O stars, the first supernova explosion does not occur for $\simeq 4$ Myr (Knödseder et al. 2002). There is no report of polarized nonthermal radio emission in the region despite many studies (although conceivably nonthermal emission from a small supernova remnant could be absorbed by free-free processes in the HII gas). The only hints of energetic activity that could be associated with a supernova remnant are several arc-like structures seen in the optical and low-frequency radio images and some high-excitation optical emission lines (§2.1). But the latter cannot be supernova remnants because there are no corresponding X-ray enhancements in the *ROSAT*

image (see the simulations of Velázquez, Koenigsberger, & Raga (2003)).

The issue is somewhat more complicated for the Rosette Nebula because of the presence of the large Monoceros Loop, a well-known old supernova remnant, in its vicinity (§2.2). However, the Monoceros Loop is far larger than the Rosette and is displaced, in the plane of the sky and probably also along the line of sight, from the region we study here. Furthermore, the X-ray morphology of the nebula is center-brightened and nicely fills the hole within the toroidal HII emission. Most supernova remnants are either edge-brightened with thermal spectra or plerionic with nonthermal spectra; only a handful are known which are center-filled with thermal gas. Finally, we recall that, like M 17, the NGC 2244 cluster is too young (1.9 Myr; §2.2) and too poor to plausibly have produced a supernova remnant.

We conclude that in both M 17 and the Rosette nebula the interpretation of the diffuse emission as arising from the interior or shock of a supernova remnant can be ruled out with considerable confidence.

6.4. O Star Winds

To investigate whether the properties of the plasma derived in §5.3 are consistent with an origin in the O star winds, we apply the stellar wind properties obtained from ultraviolet P Cygni lines for large samples of O stars (Howarth & Prinja 1989) to the O stellar populations of the two clusters under study (see Appendix A). Specifically, we apply the empirical relation $\log \dot{M} = 1.69 \log(L_*/L_\odot) - 15.41$, converting spectral subtypes to bolometric L_* following Panagia (1973). This gives an estimated total mass loss rate of $\Sigma(\dot{M}_w) \sim 3 \times 10^{-5}$ (1×10^{-5}) $M_\odot \text{ yr}^{-1}$ for the M 17 (Rosette) ionizing clusters.

The derived X-ray emitting plasma masses (Table 3) can thus be replenished by winds in $t_w \sim 5000$ yr for M 17, $t_w \sim 4000$ yr for Rosette. As this is much shorter than the lifetime of the OB stars, we infer that only a tiny fraction of the wind material generated over the OB star lifetimes is now in X-ray emitting plasma. A typical early O star wind with terminal velocity $v_w = 2500 \text{ km s}^{-1}$ would travel $r_w = v_w t_w = 12.8$ pc in M 17 (10.2 pc in Rosette) during the replenishment timescale. This wind kinetic timescale t_w is also much shorter than the plasma cooling timescale τ_{cool} , consistent with the absence of any strong cooling in the plasma as a function of distance from the O stars. Most importantly, we find that the wind kinetic energy $E_w \sim \frac{1}{2} \Sigma(\dot{M}_w) v_w^2 t_w$ is 10 (7) times the plasma thermal energy estimated above for M 17 (Rosette). Thus, only $\sim 10\%$ of the wind energy need be converted via shocks into hot thermal plasma to account for the observed X-ray emission.

7. ELABORATION OF THE OB WIND BUBBLE MODEL

From the analysis above, we find that the only plausible origin for the ~ 0.7 keV (8 MK) diffuse emission suffusing the M 17 and Rosette HII regions is the thermalization of O star wind kinetic energy. Our findings thus support the basic concept of shocked wind-swept bubbles (e.g. Pikel'ner 1968; Dyson & de Vries 1972; Weaver et al. 1977) and provide some of the first clear detections of X-ray temperature plasma in HII regions.

The calculations in §6.4 with respect to a simple wind shock model show that only about 10% of the expected wind kinetic energy is converted into observed thermal energy. The shocked wind bubbles in M 17 and Rosette are < 10 pc in radius. For comparison, the hydrodynamical calculation of Weaver et al.

(1977) predicts, for a **single** $t_* = 1$ Myr O7 star expanding into a uniform cold medium, that 30% of the wind energy appears in the X-ray temperature gas, which has a typical radius of 25 pc. Similar discrepancies are found between the relatively low displacement velocities in H α found in recently studied LMC HII regions (Nazé et al. 2001). Thus, most of the wind kinetic energy is not seen in the X-ray gas and does not expand the bubble.

Several ideas have been raised to account for the missing energy and momentum of OB winds. The most obvious possibility, for blister HII regions which are only partially confined by cold gas, is that the hot gas flows freely into the low density interstellar medium, away from the cloud. Hydrodynamical models of the expansion of stellar wind bubbles in the presence of strong density gradients are presented by Rozyczka & Tenorio-Tagle (1985) and Comerón (1997). A flow of this type is directly seen in our X-ray image of M 17 where the X-rays extend asymmetrically several parsecs to the east, and may also be present in the Rosette Nebula, where gas may flow nearly along the line of sight or through fissures in the inhomogeneous cold cloud. In the latter case, the hot medium probably quickly mixes with cloud material and becomes subject to rapid radiative cooling (McKee, van Buren, & Lazareff 1984; Capriotti & Kozminski 2001).

Another possible sink for wind kinetic energy is its conversion into a turbulent cascade in a thick boundary layer where the wind approaches the cold medium (Kahn & Breitschwerdt 1990). In this case, a high velocity shock producing X-ray plasma is weak and most of the wind energy is eventually radiated at longer wavelengths. The soft $kT \simeq 0.1$ keV (1 MK) component seen in the Rosette and M 17 diffuse emission (Table 2) may be direct evidence for rapid cooling in a post-shock or turbulent boundary layer.

A related possibility is that the wind loses most of its kinetic energy through the entrainment of cooler material close to the star (e.g. Arthur, Dyson, & Hartquist 1993; Dyson, Williams, & Redman 1995; Pittard, Hartquist, & Dyson 2001). While mass loading close to the star is unlikely in these mature HII regions which have evacuated molecular material within the stellar association, this process may be occurring at the boundaries between the X-ray and cooler gases. In the Rosette, optical images show elephant trunk structures which might be good sites for ablation and entrainment. In M 17, the stellar winds may be encountering a fissured neutral medium in the highly fragmented southern HII bar (e.g. Clayton et al. 1985; Meixner et al. 1992).

Another possibility is that the X-ray gas is produced, and the kinetic energy spent, primarily in collisions between the OB winds rather than with the exterior cold cloud. Cantó, Raga, & Rodríguez (2000) present a 3-dimensional hydrodynamical calculation of colliding OB winds which are otherwise unconfined by dense cold gas. This is an attractive model for our data, as it immediately accounts for the center-filled rather than edge-brightened morphology of the X-ray emission and for the bulk flow of the merged, shocked winds into the diffuse medium seen in M 17. They find that the X-ray emission measure integrated along the line of sight produces rather uniform emission filling the center of the cluster, even though strong pressure gradients are present at the wind-wind collision shocks. The gas temperatures over the inner parsec of the cluster are in the range 5 – 10 MK, essentially identical to the temperatures found here for the M 17 and Rosette diffuse emission.

We finally note that we do not have any clear evidence for very hard diffuse X-ray emission that might emerge from non-Maxwellian particle acceleration at a wind-cloud shock (Dorland & Montmerle 1987). The smoothed ACIS image of M 17 suggests that a hard (blue) diffuse component may be present where the hot bubble encounters the M 17SW molecular cloud (Figure 3 panels a and c), but the emission is not evident in the swiss-cheese image after point sources have been removed (Figure 4a). Our adaptive smoothing tool also shows hints of diffuse hard emission near the cluster core and the young embedded star-forming region M 17 North (Figure 4b-d) but again this is more likely to be unresolved emission from embedded point sources in these regions.

8. X-RAYS FROM HIGH-MASS STAR FORMING REGIONS (HMSFRS)

8.1. Summary of HMSFR X-ray results to date

We place the M 17 and Rosette results in the broader context of diffuse X-ray characteristics of other Galactic star forming regions to seek an understanding of the conditions necessary for large-scale X-ray emitting OB wind shocks. Results from recent *Chandra* and *XMM-Newton* observations (and one older *Einstein Observatory* result) are summarized in Table 4, listed in order of increasing reported diffuse X-ray luminosity. We caution that this should be considered a progress report rather than an authoritative tabulation¹². The regions are subject to different levels of absorption, were observed with different sensitivities (in ergs s⁻¹) and resolution (in pc), and were subject to different treatments of the T Tauri X-ray source population and diffuse emission. In most regions, the underlying T Tauri population is poorly characterized, and in some regions even the OB stars are not fully identified.

Nearby low-mass star forming regions (LMSFRs) Here we bundle together recent high-resolution studies of the Taurus-Auriga, Ophiuchi, and Perseus molecular clouds (e.g. Imanishi, Koyama, & Tsuboi 2001; Preibisch & Zinnecker 2001; Getman et al. 2002; Favata et al. 2002), along with a region of low-density star formation in the Orion cloud (Pravdo et al. 2001). Two cases of faint 10²⁸ ergs s⁻¹ diffuse (i.e. from interstellar gas rather than the immediate vicinity of young stars) X-ray emission with extent (< 10⁻³ pc) have been found in these regions, associated with small-scale shocks in high-velocity Herbig-Haro outflows (Pravdo et al. 2001; Favata et al. 2002; Bally, Feigelson & Reipurth 2003). No stars earlier than late-B are present in these images, and none of these studies report diffuse X-ray emission on parsec scales. The sensitivity limit to such emission is of order 10²⁹–10³⁰ ergs s⁻¹ pc⁻² or 10⁻³–10⁻² of that seen here in M 17 and the Rosette.

Orion Nebula (M 42) With its ‘Trapezium’ of the O6 star θ^1 C Ori surrounded by a group of O7 V to B0 V stars, a full initial mass function down to the brown dwarf regime, and an embedded cluster associated with the OMC-1 core, the Orion Nebula is the nearest HMSFR and a bright HII region. θ^1 C Ori is the principal ionizing source of the HII region and has a wind with mass loss rate $\dot{M} = 8 \times 10^{-7} M_{\odot} \text{ yr}^{-1}$ and terminal velocity $v_{\infty} = 1650 \text{ km s}^{-1}$ (Leitherer 1988). In extensive studies with *Chandra*, no diffuse emission has been reported (e.g. Schulz et al. 2001; Feigelson et al. 2002; Flaccomio et al. 2003). The upper limit to parsec-scale emission is around 10³⁰ ergs s⁻¹ pc⁻². Note, however, that the O6 star is extremely bright in X-rays and populates the wings of its point

spread function, so that faint diffuse emission could go unnoticed in the inner $\simeq 0.4$ pc radius.

Eagle Nebula (M 16) A 77 ks *Chandra* image of this region reveals over 1000 point sources, most associated with the ionizing cluster NGC 6611 (Mytyk et al. 2001). The earliest stars in the cluster (Hillenbrand et al. 1993) are the O5.5 V ((f)) star BD -13^o4923 and HD 168076 (O5 V ((f)), $v_{\infty} = 3305 \text{ km s}^{-1}$, $\dot{M} = 3 \times 10^{-6} M_{\odot} \text{ yr}^{-1}$). (For this and following O stars, we have taken terminal wind velocities v_{∞} from Prinja, Barlow, & Howarth (1990) and mass loss rates \dot{M} from Howarth & Prinja (1989), both based on studies of ultraviolet line profiles.) Our inspection of the M 16 ACIS image reveals no obvious diffuse emission at levels greater than $\sim 10^{30}$ ergs s⁻¹, although detecting any faint diffuse emission spatially coincident with the large number of point sources in the image would require more careful analysis.

Lagoon and Hourglass Nebulae (M 8) The bright bipolar HII region in M 8 known as the Hourglass Nebula was studied with *XMM-Newton* by Rauw et al. (2002). Although limited by its small extent and confusion with embedded stellar sources, soft diffuse emission with luminosity $L_x \simeq 7 \times 10^{32}$ ergs s⁻¹ and energy $kT = 0.6 \text{ keV}$ ($T = 7 \text{ MK}$) was “probably” detected from the southern lobe of the nebula. The diffuse plasma luminosity lies below this value as some contribution from the exciting star, Herschel 36 (O7 V), and lower mass stars is undoubtedly present. As we find here with M 17 and Rosette, the authors note that this X-ray luminosity is far below the 10³⁵ ergs s⁻¹ kinetic power of Her 36. An existing 60 ks *Chandra* observation of M 8 did not include the Hourglass Nebula, but a 180 ks observation that includes the Hourglass is scheduled. The *XMM-Newton* image of the larger M 8 region shows no diffuse emission associated with the main ionizing star, 9 Sgr (O4 V, $v_{\infty} = 2750 \text{ km s}^{-1}$, $\dot{M} = 5 \times 10^{-6} M_{\odot} \text{ yr}^{-1}$), and none is seen in our qualitative examination of the 60 ks *Chandra* image. Note that the other major ionizing stars of M 8, HD 165052 (O6.5 V + O6.5 V binary, $v_{\infty} = 2295 \text{ km s}^{-1}$, $\dot{M} = 3 \times 10^{-7} M_{\odot} \text{ yr}^{-1}$) lie just outside the fields of view of both the *XMM-Newton* and *Chandra* observations.

Rosette Nebula This HMSFR is discussed in detail above, with OB stars listed in Appendix A. The area of diffuse emission listed here is the size of the extraction region used to obtain the diffuse spectrum (the full ACIS-I array). The diffuse emission is soft, with spectral components at 0.1 and 0.8 keV (1 and 9 MK) and with an absorption-corrected X-ray luminosity of $L_c \leq 6 \times 10^{32}$ ergs s⁻¹ (Table 2). The true plasma emission is less than the observed value because of the uncertain, but possibly substantial, contribution of unresolved T Tauri stars (§6.2). The HII region is mainly ionized by two stars with similar wind powers: HD 46223 (O4 V ((f)), $v_{\infty} = 2910 \text{ km s}^{-1}$, $\dot{M} = 2 \times 10^{-6} M_{\odot} \text{ yr}^{-1}$) and HD 46150 (O5 V ((f)), $v_{\infty} = 2925 \text{ km s}^{-1}$, $\dot{M} = 2 \times 10^{-6} M_{\odot} \text{ yr}^{-1}$). Unlike the Trapezium and M 17, where the O stars are concentrated within the inner $\simeq 0.5$ pc, the two dominant stars in Rosette are widely separated by at least 3 pc.

RCW 38 Both soft and hard diffuse X-ray emission is reported from a 97-ks *Chandra* observation of this bright southern HII region (Wolk et al. 2002). Its ionization is dominated by a single O5 star, IRS 2. The authors fit the diffuse X-rays with a thermal bremsstrahlung plus power law model, attributing the soft bremsstrahlung component to dust-scattered X-rays and the hard power law component to some non-thermal magnetic pro-

¹² Earlier versions of this table were presented at conferences by Feigelson (2001) and Townsley et al. (2003).

cess, perhaps synchrotron emission from an embedded supernova remnant (see our discussion in §6.3). We note, however, that the diffuse spectrum in RCW 38 is similar to the integrated point source spectrum we find in M 17 (Figure 9, lower left). We fit the latter sources with a thermal plasma ($kT = 3.0$ keV, $N_H = 1.7 \times 10^{22}$ cm $^{-2}$) similar to one which fits the RCW 38 diffuse emission ($kT = 2.23$ keV, $N_H = 1.15 \times 10^{22}$ cm $^{-2}$ with low metal abundances, Wolk et al. (2002)). The authors use a deep K -band image to argue that the diffuse emission does not arise from the low-mass pre-main sequence population; it would be useful to make a comparison between the diffuse spectrum and the combined point source spectrum to elucidate the level of T Tauri contamination. We thus list in Table 4 the diffuse luminosity $L_x = 1.6 \times 10^{33}$ ergs s $^{-1}$ (which we estimated based on the count rates and spectral parameters reported in Wolk et al. (2002)) as an upper limit to the diffuse emission generated by OB winds.

Omega Nebula (M 17) These results are also discussed in detail above, with OB stars listed in Appendix A. The area of diffuse emission listed here is the size of the extraction region used to obtain the diffuse ACIS spectrum (see Figure 8a); the *ROSAT* data show that fainter, soft diffuse emission extends eastward for at least another 7 pc (see Figure 1d and Dunne03 Figure 2). The ACIS diffuse emission is soft like Rosette's, with absorption-corrected $L_c = 3.4 \times 10^{33}$ ergs s $^{-1}$. Emission outside the ACIS field of view contributes another $\sim 1 \times 10^{33}$ ergs s $^{-1}$ (Dunne03). Here, spatial structure combined with spectral comparison shows negligible contamination by low mass stars. The O stars in M 17 lack direct measurements of v_∞ and \dot{M} , but Dunne03 calculate these quantities using the method of Schaerer & de Koter (1997) and find $v_\infty = 2500$ – 3000 km s $^{-1}$, $\dot{M} = 0.3$ – 4×10^{-6} M $_\odot$ yr $^{-1}$ (see their Table 2). Ionization of the HII region is probably dominated by the obscured O4–O4 binary called Kleinmann's Anonymous Star.

Arches Cluster The Arches is one of three very massive and heavily obscured young stellar clusters in the inner 100 pc of the Galactic Center. A 51-ks *Chandra* image shows a complex morphology: most of the emission comes from two structures in the interior of the core, which may arise from either localized wind-wind collisions from close binaries or from more extended wind shocks (Yusef-Zadeh et al. 2002). The third component (A3), with $L_x \sim 1.6 \times 10^{34}$ ergs s $^{-1}$, is clearly extended several parsecs away from the stellar association, similar to the flow we see in M 17. It is this component which we list in Table 4 as a lower limit to the diffuse X-ray emission, for comparison with other regions. Note that the emission is considerably harder than that seen in Rosette or M 17 (although the fit parameters are uncertain due to the small number of counts detected) and shows a strong 6.4 keV iron fluorescent line, suggesting close interaction between the winds and ambient molecular gas. The heavy obscuration along this line of sight precludes detection of a soft component analogous to the M 17 and Rosette diffuse emission.

NGC 3603 This very dense and luminous massive stellar cluster, often considered to be the Galactic analog of the R 136 cluster at the center of 30 Doradus in the Large Magellanic Cloud, lies at a distance similar to the Arches Cluster but is less obscured. A 50-ks *Chandra* study shows hard diffuse emission with an extent $\simeq 8$ pc with $L_x \simeq 2 \times 10^{34}$ ergs s $^{-1}$ and energy ranging from $kT = 2$ to 3 keV ($T = 23$ to 35 MK), in addition to nearly 400 point sources (Moffat et al. 2002). The

diffuse component is spatially coincident with the cluster core, but the authors calculate that the underlying pre-main sequence population should be too faint to contribute substantially to the emission. The diffuse emission is attributed to the collisions of multiple stellar winds from a large population of massive (including O3–5 V and Wolf-Rayet) stars in the region.

Carina Nebula Carina is a giant HII region extending over ~ 50 pc, with an extremely rich young stellar population. It is a complicated mix of several very rich star clusters of varying ages and evolutionary states, including many very massive O3 V stars, post-main sequence Wolf-Rayet stars, and the unique eruptive η Car system. Early study with the *Einstein* satellite revealed pointlike emission from several early-type stars and a soft diffuse X-ray component, with $L_x \simeq 10^{35}$ ergs s $^{-1}$ extending over tens of parsecs (Seward & Chlebowski 1982). Dorland & Montmerle (1987) concluded that a substantial fraction of the *Einstein* emission at low energies (< 3 keV) could be explained by T Tauri stars similar to those seen in ρ Ophiuchus, while the hard X-ray contribution (> 3 keV) could be truly diffuse emission. Portions of the complex have been observed with *XMM-Newton* and *Chandra*; our examination of these images confirms the presence of diffuse emission with large-scale (> 5 pc) gradients that can not be attributed to an unresolved low-mass stellar population. Evans et al. (2003) examined early *Chandra* data and conclude that over half of the X-ray emission in Carina might come from a diffuse component. However, given the presence of many evolved massive stars, it seems likely that one or more supernovae have occurred in the region. The relative contribution of supernova remnants and OB wind shocks to the diffuse X-ray component is, in our opinion, unknown.

Other regions Closely related observations have been made which, for reasons of insufficient knowledge, we omit from Table 4. A *Chandra* observation of the heavily obscured group of ultracompact HII regions in W 3 showed over 200 point sources but no diffuse emission (Hofner et al. 2002). However, any soft emission with $kT \leq 1.5$ keV (17 MK) would be absorbed by intervening material. A faint X-ray structure with $kT \simeq 6$ keV (70 MK) and $L_x \simeq 10^{33}$ ergs s $^{-1}$ has been detected with *Chandra* in a 1×1 pc region within the Sgr B2-North HII region (Takagi, Murakami, & Koyama 2002). The absorption here is extremely high, with $N_H = 6 \times 10^{23}$ cm $^{-2}$ corresponding to over 100 magnitudes of visual absorption. It is not possible here to discriminate between emission arising from individual massive stars, many low-mass stars, and wind shocks. X-ray emission has also been found with *ROSAT* and *ASCA* in regions such as W 51, NGC 6334, and the Trifid Nebula; *Chandra* data have been recently obtained for these regions. Detailed analyses of the contribution from diffuse hot wind bubbles based on these new high-resolution images have not yet been reported, however.

8.2. Implications for X-ray Emission from OB Wind Shocks and the Structure of HII Regions

Some tentative conclusions regarding the generation of parsec-scale X-ray gas in star forming regions can be reached from these recent findings. Except for faint ($L_x \sim 10^{28}$ ergs s $^{-1}$) and localized ($< 10^{-3}$ pc) emission from some shocks in Herbig-Haro outflows (Pravdo et al. 2001; Favata et al. 2002), low-mass star forming regions show no diffuse X-rays. The terminal shocks of T Tauri winds do not produce diffuse X-rays detectable with the current generation of X-ray observatories.

Weaver et al. (1977) and similar models of wind-blown bubbles predict measurable X-ray emission associated with a single O star, even a relatively late O7 star. However the *Chandra* data show that the powerful 2000–3000 km s⁻¹ winds of **early** O stars are clearly a necessary condition to produce the shocks responsible for diffuse soft X-ray emission. Abbott (1982) showed that stellar wind power is a strong function of spectral type; late-O stars have wind power reduced by a factor of five from that of early-O stars, so HMSFRs without stars earlier than O6 may be unlikely to exhibit diffuse soft X-rays. Also, the absence of such diffuse emission in the Orion, Eagle, and Lagoon nebulae, where only one or two stars earlier than ~O6 are present, suggests another discrepancy with the Weaver et al. (1977) prediction: the O stars must be sufficiently numerous to produce detectable diffuse X-rays. The proximity of the O stars may also be important: it is possible that colliding winds, as discussed by Cantó, Raga, & Rodríguez (2000), may be more efficient at creating the kind of ‘X-ray fountain’ we see in M 17, with plasma flowing away from the exciting O star cluster.

The principal exception to these ideas is the Hourglass Nebula, where a single O7 star may have associated soft diffuse X-rays. Perhaps this star’s youth and proximity to molecular material enhances the production of soft X-rays. For parsec-scale emission, the Rosette Nebula, with two widely-separated O4–O5 stars and $L_x(\text{diffuse}) \sim 10^{32}$ ergs s⁻¹, may represent the minimal wind environment necessary to produce detectable diffuse soft X-rays. Even in this minimal case, the X-ray plasma appears to have a sufficiently strong dynamical effect to evacuate cooler material from the interior of the nebula, resulting in the annular structure of its HII gas.

The Omega Nebula, Arches Cluster, and NGC 3603 cluster have richer O star populations, producing $L_x(\text{diffuse}) \sim 10^{33} - 10^{34}$ ergs s⁻¹. Here the gas fills the interior of the photoionized HII region, pushing against the cold cloud material where it is present and flowing away from the stellar cluster where it is not. In §6.4 and Table 3, we give a quantitative analysis of this type of nebula. Less than 1% of the wind material produced over the history of the O stars is present in the nebula, suggesting that most of the wind has flowed outward, contributing to the Galactic hot interstellar medium. Some of the gas may cool, as evidenced by the 0.1 keV (1 MK) spectral component we see here. The X-ray gas in M 17 is roughly in pressure equilibrium with the cooler HII gas. The Rosette data imply that soft X-rays are present without multiple O stars in close proximity. The diffuse emission of M 17 is not concentrated around the O4–O4 binary system, implying that the collision of its component winds is not the principal source of diffuse X-rays. The ≥ 6 -fold difference in X-ray luminosity we see between Rosette and M 17 is roughly consistent with the difference in their O star populations (Rosette has 2 stars of type O6 or earlier; M 17 has 7) and their wind kinetic energies (2×10^{48} ergs in Rosette; 9×10^{48} ergs in M 17).

The Carina Nebula, where the diffuse soft X-ray luminosity is of order 10^{35} ergs s⁻¹, represents the first stages of starburst phenomena, where rich stellar clusters of a variety of ages have an enormous effect on their environment. Many powerful winds are colliding with each other, encountering the cloud edges, and quite possibly interacting with supernova remnants. The X-ray plasma is probably not relatively uniform with a simple laminar outward flow as we see in M 17. Rather, motions are likely in multiple directions, with shocks, turbulence, and strong density inhomogeneities. Such a superheated, shock-dominated

hot interstellar environment is seen in starburst superbubbles such as 30 Doradus (Chu & Mac Low 1990; Dennerl et al. 2001), the mild starburst nucleus in our Galactic Center region (Wang, Gotthelf, & Lang 2002; Munro et al. 2003), and in true nuclear starbursts such as NGC 253 (Strickland et al. 2002) and M 82 (Griffiths et al. 2000). In the latter case, the overpressure of the supernova- and wind-heated interstellar medium drives kiloparsec-scale winds of enriched material into the intergalactic medium.

A critical issue raised by these studies is the likely presence of a hard ($kT \sim 5$ keV, or 58 MK) as well as soft ($kT \simeq 0.8$ keV, or 9 MK) plasma in some portions of some HII regions. It is reported in RCW 38, NGC 3603, and the Arches Cluster but not in W 3 or the less rich stellar associations like the ONC or Rosette. In the intermediate case of M 17, unresolved hard X-rays are spatially coincident with the highest concentrations of stars; a diffuse component cannot be distinguished from an unresolved component due to the large population of faint, embedded pre-main sequence stars. In all these examples, we must be aware of the possible contamination by the population of low-mass embedded stars masquerading as diffuse gaseous emission; in regions with evolved stars or a range of cluster ages, contamination by supernova remnants must also be considered. If real, this diffuse hard component must represent a more efficient conversion of wind kinetic energy into plasma thermal energy. It may require nonlinear transport processes at the interface of the wind and molecular cloud as described by Dorland & Montmerle (1987).

One possibility for the eventual dissipation of the wind energy is that the plasma pressure overcomes the ambient pressure at a weak point, such as a low-density region at the periphery of a molecular cloud; this would be reminiscent of the ‘champagne flow’ invoked for HII regions like Orion. This is probably the case for M 17, which displays a clear flow of gas toward the boundary with the interstellar medium. Alternatively, the plasma may ‘leak’ through fissures, simply flowing past denser regions; this might be the case for Rosette, although a flow nearly along the line of sight is also possible. In both cases, the gas then escapes into the surrounding low-pressure interstellar medium, adding to the network of worms and chimneys created in the galactic disk by supernova explosions (de Avillez & Berry 2001).

If the surrounding medium is dense enough to hold the plasma, the wind energy must be efficiently dissipated at or near the periphery of the plasma bubble, since there appears to be little or no expansion of the HII shell. In the case of a steep density gradient (such that the slope is smaller than the mean free path of the plasma electrons in the HII region), Dorland & Montmerle (1987) have shown that a Maxwellian electron velocity distribution is possible, and that a high-energy electron tail efficiently takes away the wind energy via non-linear conduction. These non-thermal electrons, which would radiate hard X-rays, end up losing their energy unnoticed in the surrounding photodissociation region. This may be occurring around the embedded RCW 38 cluster, if the hard diffuse X-ray emission there is not due to a supernova remnant and/or the embedded stellar population. Another possibility for wind energy dissipation is that the hot plasma directly evaporates the surrounding medium by photoevaporation resulting from the complete absorption of the (soft) X-ray photons and/or from heating by the bremsstrahlung keV electrons.

9. CONCLUDING COMMENTS

9.1. Summary of Findings

Chandra ACIS-I images of the Rosette and M 17 HII regions in the 0.5–8 keV X-ray band reveal diffuse emission extending over several parsecs. Unlike studies with previous satellites, the high resolution of the *Chandra* mirrors and detectors and low detector noise allow faint diffuse emission to be studied in quantitative detail, even in the midst of hundreds of stellar X-ray sources. Strong arguments are presented that the emission is not attributable to supernova remnants or low-luminosity stellar sources. It is produced by plasma at $T \sim 1$ MK and ~ 10 MK with luminosities of $\leq 6 \times 10^{32}$ ergs s^{-1} in Rosette and 3.4×10^{33} ergs s^{-1} in M 17. The emission has a roughly uniform, center-brightened appearance. In Rosette, the X-ray gas surrounds the ionizing cluster, filling the hole within the well-known ring of H α and radio continuum emission. In M 17, the gas is roughly coincident (in projection) with the H α emission, brightest around the cluster core and flowing eastward for several parsecs.

9.2. Astrophysical Implications

We establish that only a small portion of the wind energy and a tiny fraction of the mass appears in the observed diffuse X-ray plasma. Although cooling into the HII component is possible, we suspect that most of the wind energy and mass of these blister HII regions flow without cooling into the low-density interstellar medium. In this case, the fate of deeply embedded winds where the stars are completely surrounded by dense molecular gas will be different than in these blister HII regions.

Together with other recent reports from *Chandra* and *XMM-Newton*, this is the first unambiguous detection of the ‘wind-swept bubble’ which has long been predicted to arise from the thermalization of OB stellar winds. We estimate that $\sim 10\%$ of the wind kinetic energy is converted to X-ray emitting plasma, although it is still not clear whether most of the dissipation occurs in wind-wind or wind-cloud shocks. We suspect that both types of shocks are present. The low-temperature spectral component suggests that some post-shock gas is cooling, but most of the gas mass and most of the kinetic energy of the winds probably stay in the form of bulk flow. This is clearly seen in M 17, where the X-ray emission flows from the core of the stellar cluster, away from the dense molecular cloud and towards low density interstellar environments. The OB wind energy is not, at least in these two cases, principally dissipated in turbulent layers or mass loading close to the O stars.

For some regions (such as Rosette), the physical conditions of the 10^4 K gas may not be well-established, if the derived pressure can change by a factor of 100 with different reasonable assumptions for geometry, clumpiness, and filling factor; compare the models of Celnik (1985) and Tsivilev et al. (2002). Derived physical parameters can also change substantially if the stellar mass loss rates change by factors of 3 or more when clumping due to turbulence is considered (Moffat & Robert 1994); this was illustrated by Dunne03 for the case of M 17. Dunne03 also showed that the presence of strong magnetic fields may inhibit heat conduction, thus reducing the X-ray luminosity in M 17 below the values predicted by the standard wind-blown bubble models.

New high-resolution optical and near-infrared images of the hydrogen line structures in HII regions are showing a rich, sub-

pc filamentary structure in the photodissociation regions (Jiang et al. 2002). This may change our ideas about the interface between the inner ten million degree plasma and the outer ten thousand degree photodissociated gas, hence about their possible exchanges of energy. The two media may well coexist in some fashion over a certain distance, a situation reminiscent of supernova remnants expanding into the interstellar medium. These considerations require that the classical ‘Strömgren sphere’ paradigm be seriously revised to better account for the existence of stellar winds.

In fact, one of the potential implications of this finding may be the need to reformulate our language and overall conception of HII regions. In M 17, the apparent outflow of X-ray gas from the NGC 6618 cluster away from the molecular cloud might be termed an ‘X-ray fountain’ or ‘X-ray champagne flow,’ in analogy to the champagne model of photoevaporation of dense gas by OB ultraviolet radiation (Tenorio-Tagle 1979). For HII regions where most of the interior volume is filled with an X-ray emitting plasma, as in M 17 and Rosette, the cooler ionized gas responsible for H α and radio continuum emission is confined to a relatively thin layer near the boundary with the molecular cloud. Thus the phrase ‘Strömgren sphere’ might be replaced with ‘Strömgren shell’ or ‘Strömgren surface.’ For M 17, this idea is supported by a recent high-resolution *JHK* image where the hydrogen line emission is mostly concentrated in filaments and a thin ‘silver lining’ around the dark cloud¹³.

The current sample of HMSFRs studied with modern X-ray instrumentation shows a large range of diffuse emission properties, with reports of both hard and soft, bright and faint emission and spatial scales of fractions of a pc² to thousands of pc². Generally, nearby, less-obscured regions show soft, faint diffuse emission filling moderate-sized, presumably wind-blown bubbles. More distant, obscured regions ionized by more early stars may sometimes exhibit hard diffuse emission, but the contribution of low-mass stellar sources is difficult to untangle. The soft component may be present but is probably absorbed. The specific character of diffuse X-rays in HMSFRs is governed by the details of star formation and the distribution of molecular material associated with each region.

In addition to clarifying HII region astrophysics, establishing the effects of OB winds on their environment is relevant for understanding the energetics of the interstellar medium on a Galactic scale. Stellar wind bubbles within an HII region can affect the evolution of later supernova remnants and superbubbles (Oey, Clarke, & Massey 2001). The integrated mechanical input of stellar winds generally exceeds that of supernova remnants over the full lifetime of a starburst event and, if efficient thermalization occurs, winds and supernovae together can power galactic superwinds (Leitherer, Robert, & Drissen 1992).

9.3. Prospects for Further Study

Chandra study of HII regions containing a variety of ionizing stellar clusters, with different wind sources and ages, and in different gaseous environments, is likely to give additional insights into the fate of OB winds. We suspect that X-ray plasma will be commonly found in HII regions when several O stars with sufficiently strong winds are present. A deeper *Chandra* observation of the Rosette Nebula is planned, both to improve the discrimination between diffuse gas and the low-mass stellar population and to search for subtle gradients in the gas properties. For example, spectral or brightness changes in the X-

¹³ <http://www.pparc.ac.uk/Nw/Press/uist.asp>

ray emission around the molecular gas would show the wind termination shock (see §7), while bright X-ray arcs between the principal O stars would reveal a wind-wind collision shock. The wind-cloud vs. wind-wind heating mechanisms can also be tested by comparing the diffuse X-ray emission in embedded clusters to those which have largely evacuated cold gas from their environment.

Study of the optical line emission from these HII regions specifically to elucidate the wind-swept bubble model would also be helpful. High-resolution imaging may confirm that the line emission is confined to a shell around the photodissociation region and does not permeate the entire volume around the ionizing cluster. Optical line spectroscopy can investigate high-velocity components in the HII region, such as knots with $\simeq 100 \text{ km s}^{-1}$ velocities reported by Meaburn & Clayton (1987) in M 17 and by Clayton et al. (1998) in Rosette, to study the dynamical influence of the winds on the cooler gas.

While hot wind-swept bubbles in HII regions have been extensively modeled for several decades, most of these studies do not make specific predictions of X-ray luminosities, temperatures, and morphologies. Notable exceptions are the studies by Dorland & Montmerle (1987), Comerón (1997), and Cantó, Raga, & Rodríguez (2000). These models are beginning to be revisited in light of the new *Chandra* findings (Stevens & Hartwell 2003). We suspect, for example, that winds with heavy mass loading or thick turbulent mixing layers are incompatible with our results while winds with strong shocks are favored, but Stevens & Hartwell (2003) favor mass-loading from the disks of pre-main sequence stars to explain the luminosity and temperature of Rosette. It would also be desirable to construct numerical three-dimensional hydrodynamical calculations with the specific configuration of wind sources and cold gaseous boundaries present in Rosette and M 17. Comparing the predicted X-ray properties to our observations should give new insights into the structure (e.g., wind-wind vs. wind-cloud) and physics of the shocks that heat HII regions to X-ray temperatures.

Support for this effort was provided by the Chandra X-ray Observatory grant G01-2008X and by NASA contract NAS8-38252. EDF thanks CEA/Saclay for hospitality during the study period. This research has made use of NASA's Astrophysics Data System and the SIMBAD database, operated at CDS, Strasbourg, France. We appreciate the insight gained through conversations with A. Dalgarno, K. Getman, C. Grant, M. Mac Low, C. McKee, J. Raymond, and C. Sarazin. We thank R. Chini for supplying data and our referee, N. Miller, for his time and helpful comments, which improved the quality of this paper. This study was a true collaboration, with equal contributions made by the first three authors in the development of the paper and substantial supporting roles played by the other authors. LKT is most grateful for this ensemble effort.

REFERENCES

- Abbott, D. C. 1982, *ApJ*, 263, 723
- Aller, L. H. 1956, *Gaseous Nebulae*, London:Chapman & Hall
- Ando, M., Nagata, T., Sato, S., Mizuno, N., Mizuno, A., Kawai, T., Nakaya, H., & Glass, I. S. 2002, *ApJ*, 574, 187
- Arnaud, K. A. 1996, *ASP Conf. Ser. 101: Astronomical Data Analysis Software and Systems V*, 5, 17
- Arthur, S. J., Dyson, J. E., & Hartquist, T. W. 1993, *MNRAS*, 261, 425
- Bally, J., Feigelson, E. D., & Reipurth, B. 2003, *ApJ*, in press
- Berghöfer, T. W. & Christian, D. J. 2002, *A&A*, 384, 890
- Brinkman, A. C. et al. 2001, *A&A*, 365, L324
- Brogan, C. L. & Troland, T. H. 2001, *ApJ*, 560, 821
- Bumgardner, T. E. 1992, M.S. thesis, Ohio State Univ.
- Cantó, J., Raga, A. C., & Rodríguez, L. F. 2000, *ApJ*, 536, 896
- Capriotti, E. R. & Kozminski, J. F. 2001, *PASP*, 113, 677
- Celnik, W. E. 1985, *A&A*, 144, 171
- Celnik, W. E. 1986, *A&A*, 160, 287
- Chartas, G., Brandt, W. N., Gallagher, S. C., & Garmire, G. P. 2002, *ApJ*, 579, 169
- Chini, R., Elsaesser, H., & Neckel, T. 1980, *A&A*, 91, 186
- Chini, R., Nielbock, M., & Beck, R. 2000, *A&A*, 357, L33
- Chini, R. & Wargau, W. F. 1998, *A&A*, 329, 161
- Chu, Y. & Mac Low, M. 1990, *ApJ*, 365, 510
- Chu, Y., Guerrero, M. A., & Gruendl, R. A. 2002, in *IAU Symposium No. 209, "Planetary Nebulae: Their Evolution and Role in the Universe"* (San Francisco:ASP), in press (astro-ph/0202509)
- Chu, Y.-H. 2002, in *IAU Symposium 212, "A Massive Star Odyssey: From Main Sequence to Supernova"* (eds. K. A. van der Hucht et al.) (San Francisco:ASP), in press (astro-ph/0208172)
- Chu, Y.-H., Gruendl, R. A., & Guerrero, M. A. 2003, *Revista Mexicana de Astronomia y Astrofisica Conference Series*, 15, 62
- Clayton, C. A., Ivchenko, V. N., Meaburn, J., & Walsh, J. R. 1985, *MNRAS*, 216, 761
- Clayton, C. A., Meaburn, J., Lopez, J. A., Christopoulou, P. E., & Goudis, C. D. 1998, *A&A*, 334, 264
- Comerón, F. 1997, *A&A*, 326, 1195
- Cox, P., Deharveng, L., & Leene, A. 1990, *A&A*, 230, 181
- Davies, R. D., Elliott, K. H., Goudis, C., Meaburn, J., & Tebbutt, N. J. 1978, *A&AS*, 31, 271
- de Avillez, M. A. & Berry, D. L. 2001, *MNRAS*, 328, 708
- Dennerl, K. et al. 2001, *A&A*, 365, L202
- Dorland, H., Montmerle, T., & Doom, C. 1986, *A&A*, 160, 1
- Dorland, H. & Montmerle, T. 1987, *A&A*, 177, 243
- Dunne, B. C., Chen, C.-H., Lowry, J. D., Townsley, L. K., Gruendl, R. A., Guerrero, M. A., & Chu, Y.-H. 2003, *ApJ*, in press (astro-ph/0302579)
- Dyson, J. E. 1977, *A&A*, 59, 161
- Dyson, J. E. & de Vries, J. 1972, *A&A*, 20, 223
- Dyson, J. E., Williams, R. J. R., & Redman, M. P. 1995, *MNRAS*, 277, 700
- Ebisawa, K., Maeda, Y., Kaneda, H., & Yamauchi, S. 2001, *Science*, 293, 1633
- Evans, N. R., Seward, F. D., Krauss, M. I., Isobe, T., Nichols, J., Schlegel, E. M., & Wolk, S. J. 2003, *ApJ*, accepted (astro-ph/0301485)
- Favata, F., Fridlund, C. V. M., Micela, G., Sciortino, S., & Kaas, A. A. 2002, *A&A*, 386, 204
- Feigelson, E. D. 2001, *ASP Conf. Ser. 234: X-ray Astronomy 2000*, 131
- Feigelson, E. D., Broos, P., Gaffney, J. A., Garmire, G., Hillenbrand, L. A., Pravdo, S. H., Townsley, L., & Tsuboi, Y. 2002, *ApJ*, 574, 258
- Felli, M., Massi, M., & Churchwell, E. 1984, *A&A*, 136, 53
- Flaccomio, E., Damiani, F., Micela, G., Sciortino, S., Harnden, F. R., Murray, S. S., & Wolk, S. J. 2003, *ApJ*, 582, 382
- Fountain, W. F., Gary, G. A., & Odell, C. R. 1979, *ApJ*, 229, 971
- Freeman, P. E., Kashyap, V., Rosner, R., & Lamb, D. Q. 2002, *ApJS*, 138, 185
- García, B. & Mermilliod, J. C. 2001, *A&A*, 368, 122
- Getman, K. V., Feigelson, E. D., Townsley, L., Bally, J., Lada, C. J., & Reipurth, B. 2002, *ApJ*, 575, 354
- Glushkov, Y. I. 1998, *Astron. Reports*, 42, 137
- Goldwurm, A., Caraveo, P. A., & Bignami, G. F. 1987, *ApJ*, 322, 349
- Gregorio-Hetem, J., Montmerle, T., Casanova, S., & Feigelson, E. D. 1998, *A&A*, 331, 193
- Griffiths, R. E., Ptak, A., Feigelson, E. D., Garmire, G., Townsley, L., Brandt, W. N., Sambruna, R., & Bregman, J. N. 2000, *Science*, 290, 1325
- Hanson, M. M., Howarth, I. D., & Conti, P. S. 1997, *ApJ*, 489, 698
- Henning, T., Klein, R., Launhardt, R., Lemke, D., & Pfau, W. 1998, *A&A*, 332, 1035
- Hensberge, H., Pavlovski, K., & Verschueren, W. 2000, *A&A*, 358, 553
- Hillenbrand, L. A., Massey, P., Strom, S. E., & Merrill, K. M. 1993, *AJ*, 106, 1906
- Hillenbrand, L. A. 1997, *AJ*, 113, 1733
- Hofner, P., Delgado, H., Whitney, B., Churchwell, E., & Linz, H. 2002, *ApJ*, 579, L95
- Høg, E. et al. 2000, *A&A*, 355, L27
- Howarth, I. D. & Prinja, R. K. 1989, *ApJS*, 69, 527
- Imanishi, K., Koyama, K., & Tsuboi, Y. 2001, *ApJ*, 557, 747
- Jaffe, T. R., Bhattacharya, D., Dixon, D. D., & Zych, A. D. 1997, *ApJ*, 484, L129
- Jiang, Z. et al. 2002, *ApJ*, 577, 245
- Johnson, H. L. 1962, *ApJ*, 136, 1135
- Johnson, C. O., Depree, C. G., & Goss, W. M. 1998, *ApJ*, 500, 302
- Kaastra, J. S. 1992, "An X-Ray Spectral Code for Optically Thin Plasmas," Internal SRON-Leiden Report, Version 2.0
- Kahn, F. D. & Breitschwerdt, D. 1990, *MNRAS*, 242, 209
- Kassis, M., Deutsch, L. K., Campbell, M. F., Hora, J. L., Fazio, G. G., & Hoffmann, W. F. 2002, *AJ*, 124, 1636
- Kleinmann, D. E. 1973, *Astrophys. Lett.*, 13, 49
- Knödseder, J., Cerviño, M., Le Duigou, J.-M., Meynet, G., Schaerer, D. & von Ballmoos, P. 2002, *A&A*, 390, 945
- Kuznetsov, V. I., Boutenko, G. Z., Lazorenko, G. A., & Lazorenko, P. F. 2000, *A&AS*, 142, 389
- Lada, C. J., Depoy, D. L., Merrill, K. M., & Gatley, I. 1991, *ApJ*, 374, 533
- Lamers, H. J. G. L. M. & Cassinelli, J. P. 1999, *Introduction to Stellar Winds*, Cambridge University Press
- Lamers, H. J. G. L. M. & Leitherer, C. 1993, *ApJ*, 412, 771
- Landi, E. & Landini, M. 1999, *A&A*, 347, 401
- Leahy, D. A. 1985, *MNRAS*, 217, 69
- Leitherer, C. 1988, *ApJ*, 326, 356
- Leitherer, C., Robert, C., & Drissen, L. 1992, *ApJ*, 401, 596
- Li, J. Z., Wu, C. H., Chen, W. P., Rector, T., Chu, Y. H., & Ip, W. H. 2002, *AJ*, 123, 2590
- Liedahl, D. A., Osterheld, A. L., & Goldstein, W. H. 1995, *ApJ*, 438, L115
- Lygå, G. 1987, *Computer Based Catalogue of Open Cluster Data*, 5th ed. (Strasbourg: CDS)
- Mac Low, M.-M. 2000, *Revista Mex. Astron. Astrofisica Conf. Series*, 9, 273
- Massey, P., Johnson, K. E., & Degioia-Eastwood, K. 1995, *ApJ*, 454, 151
- Mathews, W. G. 1966, *ApJ*, 144, 206
- Mathews, W. G. & O'Dell, C. R. 1969, *ARA&A*, 7, 67
- Matsuzaki, K., Sekimoto, Y., Kamae, T., Yamamoto, S., Tatematsu, K., & Umemoto, T. 1999, *Astron. Nach.*, 320, 323
- McCullough, P. R. 2000, *PASP*, 112, 1542
- McKee, C. F., van Buren, D., & Lazareff, B. 1984, *ApJ*, 278, L115
- Meaburn, J. & Clayton, C. A. 1987, *MNRAS*, 229, 253
- Meixner, M., Haas, M. R., Tielens, A. G. G. M., Erickson, E. F., & Werner, M. 1992, *ApJ*, 390, 499
- Menzel, D. H. 1937, *ApJ*, 85, 330
- Mewe, R., Lemen, J. R., & van den Oord, G. H. J. 1986, *A&AS*, 65, 511
- Moffat, A. F. J. et al. 2002, *ApJ*, 573, 191
- Moffat, A. F. J. & Robert, C. 1994, *ApJ*, 421, 310
- Monet, D. B. A. et al. 1998, *VizieR Online Data Catalog*, 1252
- Morrison, R. & McCammon, D. 1983, *ApJ*, 270, 119
- Morton, D. C. 1967, *ApJ*, 147, 1017
- Muno, M. P. et al. 2003, *ApJ*, accepted (astro-ph/0301371)
- Mytyk, A. M., Daniel, K. J., Gagne, M., & Linsky, J. L. 2001, *American Astronomical Society Meeting*, 199, #04.08
- Nazé, Y., Chu, Y., Points, S. D., Danforth, C. W., Rosado, M., & Chen, C.-H. R. 2001, *AJ*, 122, 921
- Nielbock, M., Chini, R., Jütte, M., & Manthey, E. 2001, *A&A*, 377, 273
- Nilakshi, Sagar, R., Pandey, A. K., & Mohan, V. 2002, *A&A*, 383, 153
- Odegard, N. 1986, *ApJ*, 301, 813
- Oey, M. S., Clarke, C. J., & Massey, P. 2001, "Dwarf Galaxies and their Environment" (eds. K. de Boer, R.-J. Dettmar, & U. Klein) (Shaker Verlag), 181
- Ogura, K. & Ishida, K. 1976, *PASJ*, 28, 35
- Ogura, K. & Ishida, K. 1981, *PASJ*, 33, 149
- Oliver, R. J., Masheder, M. R. W., & Thaddeus, P. 1996, *A&A*, 315, 578
- Panagia, N. 1973, *AJ*, 78, 929
- Park, B. & Sung, H. 2002, *AJ*, 123, 892
- Pérez, M. R. 1991, *Revista Mex. Astron. Astrofisica*, 22, 99
- Phelps, R. L. & Lada, E. A. 1997, *ApJ*, 477, 176
- Pikel'ner, S. B. 1968, *Astrophys. Lett.*, 2, 97
- Pittard, J. M., Hartquist, T. W., & Dyson, J. E. 2001, *A&A*, 373, 1043
- Pravdo, S. H., Feigelson, E. D., Garmire, G., Maeda, Y., Tsuboi, Y., & Bally, J. 2001, *Nature*, 413, 708
- Preibisch, T. & Zinnecker, H. 2001, *AJ*, 122, 866
- Prinja, R. K., Barlow, M. J., & Howarth, I. D. 1990, *ApJ*, 361, 607
- Rauw, G., Nazé, Y., Gosset, E., Stevens, I. R., Blomme, R., Corcoran, M. F., Pittard, J. M., & Runacres, M. C. 2002, *A&A*, 395, 499
- Rozyczka, M. & Tenorio-Tagle, G. 1985, *A&A*, 147, 209
- Schneider, N., Stutzki, J., Winniewisser, G., Poglitsch, A., & Madden, S. 1998, *A&A*, 338, 262
- Seward, F. D. & Chlebowski, T. 1982, *ApJ*, 256, 530
- Schulz, N. S., Canizares, C. R., Huenemoerder, D., & Lee, J. C. 2000, *ApJ*, 545, L135
- Schulz, N. S., Canizares, C., Huenemoerder, D., Kastner, J. H., Taylor, S. C., & Bergstrom, E. J. 2001, *ApJ*, 549, 441
- Schaerer, D. & de Koter, A. 1997, *A&A*, 322, 598
- Silich, S. A., Tenorio-Tagle, G., Terlevich, R., Terlevich, E., & Netzer, H. 2001, *MNRAS*, 324, 191
- Smith, R. K., Brickhouse, N. S., Liedahl, D. A., & Raymond, J. C. 2001, *ApJ*, 556, L91
- Snowden, S. L., Egger, R., Finkbeiner, D. P., Freyberg, M. J., & Plucinsky, P. P. 1998, *ApJ*, 493, 715

- Stevens, I. R. & Hartwell, J. M. 2003, MNRAS, 339, 280
 Strickland, D. K. & Stevens, I. R. 1999, MNRAS, 306, 43
 Strickland, D. K., Heckman, T. M., Colbert, E. J. M., Hoopes, C. G., & Weaver, K. A. 2002, in IAU Symposium 212, "A Massive Star Odyssey: From Main Sequence to Supernova" (eds. K. A. van der Hucht et al.) (San Francisco:ASP), in press (astro-ph/0207177)
 Strömberg, B. 1939, ApJ, 89, 526
 Subrahmanyan, R. & Goss, W. M. 1996, MNRAS, 281, 239
 Takagi, S., Murakami, H., & Koyama, K. 2002, ApJ, 573, 275
 Tenorio-Tagle, G. 1979, A&A, 71, 59
 Townsley, L. K., Broos, P. S., Nousek, J. A., & Garmire, G. P. 2001, Nuclear Instr. & Methods, 486, 751
 Townsley, L. K., Broos, P. S., Chartas, G., Moskalenko, E., Nousek, J. A., & Pavlov, G. G. 2001, Nuclear Instr. & Methods, 486, 716
 Townsley, L. K., Broos, P. S., Chu, Y.-H., Feigelson, E. D., Garmire, G. P., Getman, K. V., & Montmerle, T. 2003, Revista Mexicana de Astronomia y Astrofisica Conference Series, 15, 190
 Tsvilev, A. P. & Krasnov, V. V. 1999, Astronomy Reports, 43, 511
 Tsvilev, A. P., Poppi, S., Cortiglioni, S., Palumbo, G. G. C., Orsini, M., & Maccaferri, G. 2002, New Astronomy, 7, 449
 Tsuboi, Y., Koyama, K., Murakami, H., Hayashi, M., Skinner, S., & Ueno, S. 1998, ApJ, 503, 894
 Velázquez, P. F., Koenigsberger, G., & Raga, A. C. 2003, ApJ, 584, 284
 Walborn, N. R. et al. 2002, AJ, 123, 2754
 Wallerstein, G. & Jacobsen, T. S. 1976, ApJ, 207, 53
 Wang, Q. D., Gotthelf, E. V., & Lang, C. C. 2002, Nature, 415, 148
 Weaver, R., McCray, R., Castor, J., Shapiro, P., & Moore, R. 1977, ApJ, 218, 377
 Weisskopf, M. C., Brinkman, B., Canizares, C., Garmire, G., Murray, S., & Van Speybroeck, L. P. 2002, PASP, 114, 1
 Welsh, B. Y., Sfeir, D. M., Sallmen, S., & Lallement, R. 2001, A&A, 372, 516
 Williams, J. P., Blitz, L., & Stark, A. A. 1995, ApJ, 451, 252
 Wolk, S. J., Bourke, T. L., Smith, R. K., Spitzbart, B., & Alves, J. 2002, ApJ, 580, L161
 Yusef-Zadeh, F., Law, C., Wardle, M., Wang, Q. D., Fruscione, A., Lang, C. C., & Cotera, A. 2002, ApJ, 570, 665

10. APPENDIX A: MASSIVE STARS IN M 17 AND ROSETTE

Tables 5 and 6 give properties of the O and early B stars (through B3) in NGC 6618, the cluster exciting M 17, and NGC 2244, the cluster exciting the Rosette Nebula, respectively. The tables are ordered by spectral type. All values are obtained from the literature except for the final column, which indicates whether the star is detected in our *Chandra* ACIS images. There may be additional early-type members of NGC 6618; visual studies of this cluster are complicated by heavy obscuration and confusion with the bright HII region and near-infrared studies have not covered the entire cluster, which may extend up to 25' (~ 11.6 pc) in diameter (Pérez 1991). In Rosette, the census of early stars is probably more complete because the cluster core is less absorbed. Some of the stars listed in Table 6, however, lie well outside the cluster coronal radius of 7.95 pc ($\sim 19.5'$) measured by Nilakshi et al. (2002) and thus may not be members of NGC 2244. They may be associated with other star-forming regions in the Mon OB2 association or the RMC, since they possess other properties that are consistent with NGC 2244 cluster membership (Kuznetsov et al. 2000).

11. APPENDIX B: ACIS DATA REDUCTION PROCEDURE

Our ACIS data reduction begins with the Level 1 event list ('evt1 file') and associated files (e.g., the telescope aspect solution, contained in the 'asol1' file). We require Level 1 data products because they contain information that is unavailable in the more highly processed Level 2 files. Many of the diagnostic plots described below are easily generated by *Event Browser*, part of the 'Tools for ACIS Review and Analysis' (TARA) package developed by Patrick Broos and other members of the ACIS team and available to all interested users¹⁴.

The first step is to improve the absolute astrometry of the field by registering X-ray point sources with (typically) visual catalogs of high astrometric precision. If enough matches are found in the field, we use the Tycho 2 catalog of Hipparcos positions (Høg et al. 2000). If the field contains few Tycho matches (as is the case for M 17) we can usually obtain enough matches with the USNO A2.0 catalog (Monet et al. 1998) to improve the positions. Preliminary *Chandra* source positions are obtained by running *wavdetect* (Freeman et al. 2002) on a Level 2 event list, including only the central part of the ACIS-I array for speed and because the small PSFs in this region will yield better X-ray positions. We then compute the median offset between X-ray and visual positions in RA and Dec separately, discarding outliers that are likely due to mismatched sources. The astrometry of the observation is adjusted by offsetting the RA and Dec columns in the aspect file, offsetting the nominal pointing coordinates, and reprojecting the event data.

We remove the pixel randomization when the events are reprojected; in our experience, any observation longer than a few ksec samples enough pixels due to spacecraft dither that any pixel-to-pixel gain variations are already averaged out, and the best possible positions and sharpest PSFs are critical here, to enable source matching with catalogs from other wavebands. Note that the sky coordinates (x,y) of the events will not change (except for the removal of the pixel randomization); reprojection simply moves the x/y system on the sky (in both asol1 and evt1 files). A comparison of the old and new positions is made by examining the distribution of the distance each event moved. The pixel randomization consists of uniform random numbers [-0.5,0.5] added to the CCD chip coordinates. With a non-zero roll angle, the randomization in x/y coordinates is not a uniform distribution but it should have a characteristic shape, with a maximum value of $\sqrt{0.5^2 + 0.5^2} = 0.7$ pixels.

The data are then examined for possible processing errors. The set of flight event grades [24, 66, 107, 214, 255] are removed in the onboard processing (they are not telemetered to the ground). Thus, the appearance of many events with these grades in the Level 1 data strongly suggests a processing error, such as the use of an incorrect bias. If the field contains a very bright source then we have the opportunity to look for a variety of problems in the aspect solution. By plotting event x and y positions versus event arrival time for a small region around the brightest source we may look for "movement" of the source across the sky. Incomplete de-dithering might produce periodic movement; aspect camera problems might produce jumps in the position; motion of the Science Instrument Module at the beginning or end of the observation will make the source appear to run off the field completely.

If the data were obtained in "Timed Event, Very Faint" mode, each event consists of a 5×5 pixel event island. Code was developed by Alexey Vikhlinin (CXC)¹⁵ to use the outer pixels in this island as a way to reduce background. This routine sets a status bit that flags events with high outer pixels. It will flag good events from bright sources as well as bad events, so it must be used with caution. For appropriate data, this routine is applied at this stage of the processing and the event list is filtered to remove flagged events. As with all filtering steps, we carefully examine the events that are discarded to make sure that the filtering was appropriate and was

¹⁴ <http://www.astro.psu.edu/xray/docs/TARA/>

¹⁵ http://hea-www.harvard.edu/alexey/vf_bg/vfbg.html

applied correctly.

The data are then corrected for radiation-induced charge transfer inefficiency (CTI) using the method developed at Penn State (Townsend et al. 2002a). Correcting for CTI improves spectral resolution of extended sources by $\sim 20\text{--}40\%$. This is illustrated in Figure 10, which gives the energy resolution of ACIS-I CCDs as a function of CCD row number both before and after CTI correction, shown using the FWHM of the Al $K\alpha$ and Mn $K\alpha$ calibration lines in the ACIS External Calibration Source (ECS) (Townsend et al. 2002b).

The latest release of CIAO (November 2002, Version 2.3) now includes a CTI corrector for front-illuminated (FI) CCDs, developed by the MIT ACIS group and the CXC. It employs the same forward-modeling approach used in the Penn State corrector, although the implementation and details of the model are different. This code was not available when the M 17 and Rosette data were analyzed and does not apply to back-illuminated (BI) devices, so the Penn State corrector was used; which code we use in the future will depend on performance, as assessed by CTI correction of the ACIS ECS data. These calibration observations are made every orbit, as a way to monitor CTI and other aspects of ACIS performance. They can be used as a check on the uniformity of the energy calibration across the field and are available via the Provisional Data Retrieval Interface¹⁶. The CXC can provide users with the observation identification number (“obsid”) of the calibration observations most appropriate for a given celestial observation.

To check the Penn State CTI corrector performance on the M 17 data, we ran the corrector on the closest ECS data, observation ID 61277. A plot of chipy vs. energy showed that the corrector still worked well for improving spectral resolution; it was tuned using data from January 2000 through January 2001, so it was prudent to check its performance for the M 17 data which were obtained in March 2002. This test did reveal a problem, however: the corrector was not doing a good job of regularizing the gain across the CCD, so the event energies showed a clear decline of $\sim 1\%$ from the bottom of the CCD to the top. This test motivated us to include the time-dependence of the CTI as measured by Catherine Grant¹⁷ in the Penn State CTI corrector. This new code restored the flat gain across the CCDs for this observation; in fact, this time-dependent corrector surpasses the original corrector for *all* ACIS observations made at a focal plane temperature of -120C , for both FI and BI devices. Analysis products developed for use with the original Penn State CTI corrector (RMF and QEU files) are still valid for the time-dependent corrector; these products and the corrector code are available online¹⁸.

The events are then filtered in various ways. The standard grade filter (retaining only *ASCA*-type grades 0, 2, 3, 4, and 6) is applied and events with bad grades are examined to make sure that they are truly bad (for example, legitimate X-ray point sources might show up in an image made of the bad grades—this would be an indication of photon pile-up in these sources and a warning to the user that these sources must be analyzed more carefully). The Level 1 event lists include a “status” column containing 32 single-bit flags representing various reasons why an event may be deemed undesirable¹⁹. Most observers will want to respect most of these flags, removing events which have a flag value of 1. There is one notable exception: bits 16–19 are set by the pipeline tool *acis_detect_afterglow* in an attempt to identify spurious events due to cosmic ray afterglows. This tool suffers the problem of flagging real events from even moderately bright sources²⁰. By simply applying a [status=0] filter or by using the Level 2 event list, significant numbers of legitimate events from point sources will be discarded. Again, this behavior is not restricted to bright point sources. To avoid this problem, at this stage of the processing we follow the uncontroversial status flags but ignore flags 16–19 by applying this filter: [status=000000000000xxxx00000000000000000].

The CXC distributes a ‘flight timeline’ (flt1.fits) file containing Good Time Interval (GTI) tables which designate certain time intervals deemed “bad” by the CXC pipelines. We do not know exactly what criteria are used by the CXC to determine these Good Time Intervals, but many observations contain small gaps in the aspect solution which are recorded in the “flight timeline.” Filtering with these GTI tables is applied as part of the Level 2 processing, and we apply it here. We search for additional aspect glitches by examining the *acis.asol1* file, a timeseries of the absolute pointing (RA, Dec, Roll angle).

Due to solar activity, the particle background can increase substantially over short timescales. We search for these background flares, which are especially troublesome on BI CCDs, by examining lightcurves from each CCD using the CXC’s *lightcurve* tool. We then modify the GTI files and apply them to the event list to exclude times containing flares. We always verify that the cleaned data no longer show flares by re-computing the lightcurves.

The data are then searched for hot columns or hot pixels that are not removed by the standard processing. These can be found by careful examination of each CCD (in chip coordinates); the image must retain 1-pixel binning in order to see the hot columns. Another good way to find hot columns is to make a histogram of events as a function of the CHIPX coordinate; columns with too many events are then easily noticed. It is important to check the energies at which these bad columns go away. We have found that most are gone above 0.7 keV, virtually all are gone above 1 keV, and absolutely all are gone above 2 keV. The worst CCD by far is the noisy CCD8 (S4). We find that we almost always have to filter CCD0 (I0), column 3, to remove events below 700 eV. Also, there is a hot pixel in CCD6 (S2), at chip coordinates (766,501). Note that any spatial filtering done here is *not* reflected in the bad pixel file and is thus not accounted for in ARF or exposure map calculations. For making smoothed images, it is better to remove the bad columns and suffer an imperfect exposure map than to leave them in, especially if soft extended emission might be present or there are other reasons to work in very soft bands (< 1 keV).

CIAO provides the command *acisreadcorr* to remove readout streaks due to bright sources²¹. We do not use it in this recipe, however, because we are mainly concerned with large fields full of point sources. In these fields, it is highly likely that other point

¹⁶ <http://cxc.harvard.edu/cgi-gen/cda/retrieve5.pl>

¹⁷ <http://space.mit.edu/~cgrant/cti/cti120.html>

¹⁸ <http://www.astro.psu.edu/users/townsend/cti>

¹⁹ See http://space.mit.edu/~gea/docs/acis_event_status_bits.html for the definitions of these flags.

²⁰ See <http://www.astro.psu.edu/users/tsuboi/FlaringPixel/> for an explanation of this problem.

²¹ <http://asc.harvard.edu/ciao/ahelp/acisreadcorr.html>

sources fall under the readout streak of the bright one. The *acisreadcorr* operation removes *all* the events in the streak and replaces them with artificial data according to some spectral shape of the nominal background that the user provides.

This filtered event list is then examined to make sure that it still contains a GTI table for each CCD and that appropriate FITS header keywords are present and set to the right values. A very coarse energy filter is then applied to remove events that we know are background. These energy limits (0–10.5 keV) are well outside the range that will be used for spectral fitting. This needs to be done here even if it was done before CTI correction, because the corrector moves some events up to very high energies when it corrects cosmic rays.

Note that these data still have flaring pixels in them, because applying the flaring pixel filter removes good events. These data have not been band-limited (filtered strongly by energy or PI). Further filtering by energy is useful when making images and for timing analysis, but must not be done for spectral analysis because the low and high energy ranges specified will, in general, fall in the middle of PI or PHA bins, which are used to construct spectra. Generally speaking, the user should specify the energy range over which spectra will be fit directly in the fitting package, rather than by band-limiting the data. The flaring pixel filter and an energy filter to minimize background are applied before source-searching is done.

12. APPENDIX C: AN ALTERNATIVE METHOD FOR ADAPTIVE-KERNEL IMAGE SMOOTHING

The smoothed images shown in Figures 4 and 7 were constructed using a simple adaptive kernel smoothing method. The smoothing kernels consist of the null kernel

$$k(0, i, j) = \delta(i, j) = 1 \text{ when } i = 0, j = 0 \text{ (and 0 otherwise)}$$

which produces no smoothing, plus a family of 2-D Gaussians with integer sigma values $r = \{1, 2, 3, \dots\}$,

$$k(r, i, j) = \exp \frac{-i^2 - j^2}{2r^2} .$$

For a particular kernel size, $r = R$, the flux at position (X, Y) is estimated as

$$flux(X, Y) = \frac{counts}{exposure} \quad (1)$$

where

$$counts = \sum_{x \in Obs} \sum_{y \in Obs} k(R, x - X, y - Y) image(x, y) ,$$

$$exposure = \sum_{x \in Obs} \sum_{y \in Obs} k(R, x - X, y - Y) emap(x, y) ,$$

Obs is the set of pixels in the ‘observed’ region (positive exposure) of the scene, *image* is the integer-valued image of observed counts, and *emap* is the exposure map.

To derive an estimate of the error on the flux value, we first note that each pixel in our observed counts image, *image*(x, y), is of course a sample from an unknown underlying Poisson distribution associated with that pixel. We make the simplifying assumption that all the pixels under the kernel have the **same** true flux (which we just estimated). By multiplying that flux by the pixel’s exposure value, we then compute the mean number of counts that should be observed in each pixel if the image was repeatedly observed:

$$mean(x, y) = flux(X, Y) emap(x, y) .$$

Each pixel’s (Poisson) variance is assumed to be that mean value. We then propagate the variances of the distributions through the linear equation (1) in the usual way to obtain an error for our flux estimate:

$$error = \frac{\sqrt{\sum_{x \in Obs} \sum_{y \in Obs} [k(R, x - X, y - Y)]^2 flux(X, Y) emap(x, y)}}{exposure} .$$

The flux and flux error are used to define a simple ‘significance’ value,

$$\begin{aligned} significance &= \frac{flux}{error} \\ &= \frac{\sum_{x \in Obs} \sum_{y \in Obs} k(R, x - X, y - Y) image(x, y)}{\sqrt{\sum_{x \in Obs} \sum_{y \in Obs} [k(R, x - X, y - Y)]^2 flux(X, Y) emap(x, y)}} \end{aligned}$$

which increases as r increases since more counts are encompassed under the kernel. The observer supplies a significance threshold, and at each position (X, Y) the flux is estimated using the smallest kernel size, r , that produces a significance exceeding the threshold. Thus, regions of low flux are more heavily smoothed than regions of higher flux. The significance threshold controls the overall level of smoothing. A map of the kernel sizes chosen is returned by the smoothing program.

Application of the kernel to the exposure map in Equation (1) is required for accurate smoothing of any wide-field ACIS image because the exposure varies significantly due to chip gaps and bad regions of the detector, as shown in the example swiss-cheese exposure map in Figure 11. The algorithm naturally handles unobserved regions, such as areas explicitly masked by the observer and areas outside the field of view of ACIS, because those zero-count and zero-exposure pixels do not affect either the flux or flux error computations. As you would expect, an unobserved region tends to cause neighboring observed regions to be more heavily smoothed since a larger kernel must be used to find an adequate number of counts. Note that the algorithm will estimate a flux for unobserved pixels (zero exposure) using the nearby observed regions, as in Figures 4d and 7d. This is of course a form of interpolation.

The smoothing program recognizes a negative value in the exposure map as a flag specifying that the position is 'off-field,' meaning that no flux estimate should be computed there. We flag unobserved pixels in this way for several purposes: (1) Pixels outside the field of view of ACIS represent regions of the sky totally unobserved. Estimates of the sky flux on those regions are inappropriate since they would be extrapolations. It is desirable to include in this 'off-field' category pixels at the edge of the detector which have very small exposure (due to dithering) because normalization by very small exposure values leads to noisy results. The off-field category can be most easily defined by simply thresholding the original exposure map (prior to application of the swiss-cheese mask regions). (2) In Figures 4b and 7b, we flagged as off-field all the pixels that were masked by the observer, preventing any interpolation over the holes. (3) In Figures 4c and 7c, we flagged as off-field those masked pixels that were more than a certain distance from any on-field pixel. This compromise approach fills in many small holes that are distracting to the eye, while avoiding making gross interpolations across large masked regions.

This algorithm has been implemented as the IDL program *adaptive_density_2d.pro* and is part of the publicly-available TARA software package mentioned in Appendix B.

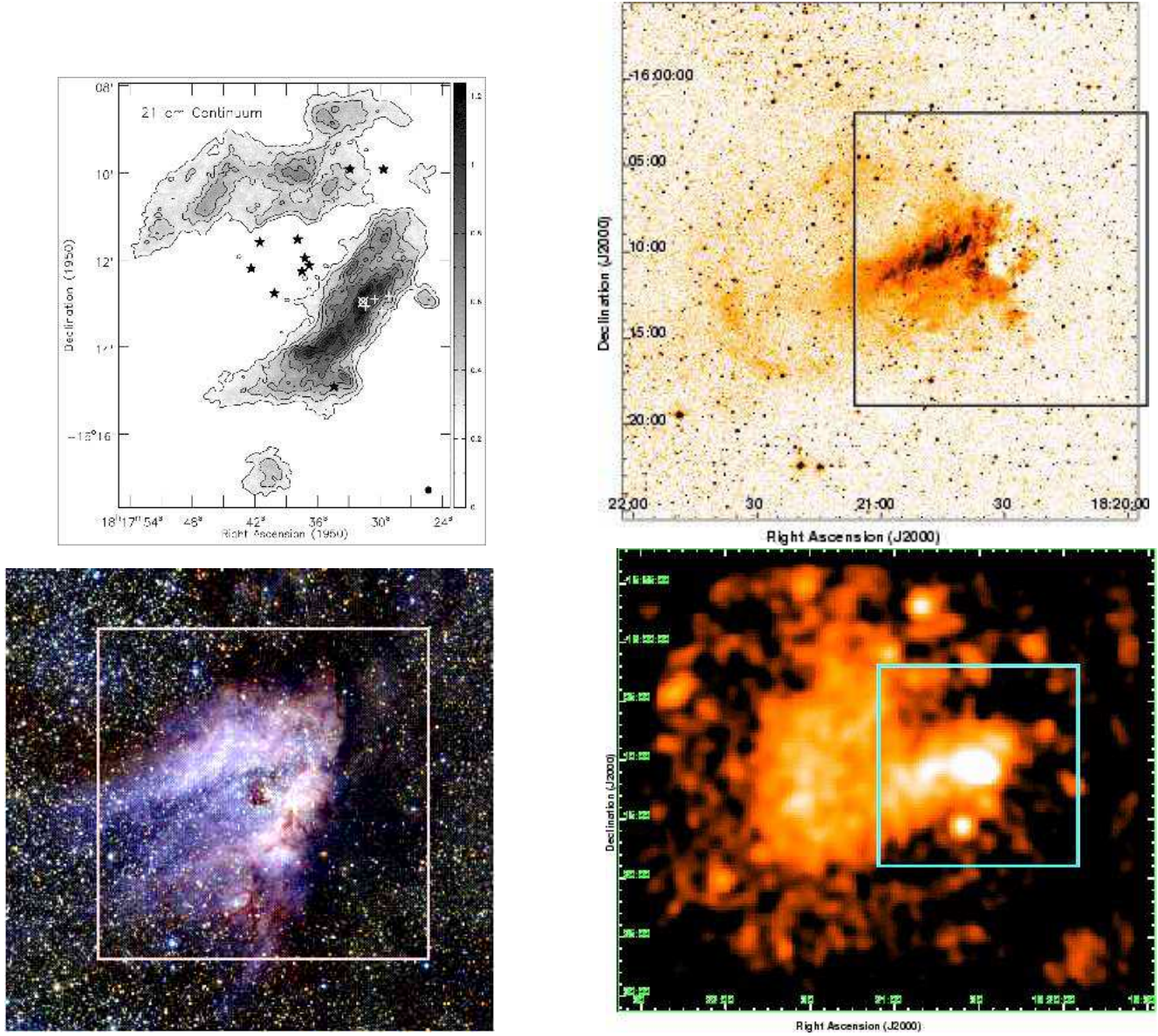


FIG. 1.— Multiwavelength views of M 17: (a) Radio continuum map showing HII gas with respect to the brightest O stars (filled stars), the embedded ultracompact HII region (circle) and nearby molecular masers (plusses and cross), from Brogan & Troland (2001). (b) Digitized Sky Survey image showing the stellar field and H α emission from the HII region, with the approximate location of the $\sim 17' \times 17'$ ACIS-I array in our observation outlined in black. (c) *JHK* image of the central region (roughly $23' \times 25'$) from the 2MASS survey, showing the NGC 6618 stellar cluster and ionized gas surrounded by the dark molecular cloud (Atlas Image courtesy of 2MASS/UMass/IPAC-Caltech/NASA/NSF); again the approximate location of the ACIS-I array is overlaid. (d) *ROSAT* PSPC X-ray image of M 17 and vicinity, with the approximate location of the ACIS-I array outlined in blue. In these and all following images, North is up and East to the left unless otherwise noted.

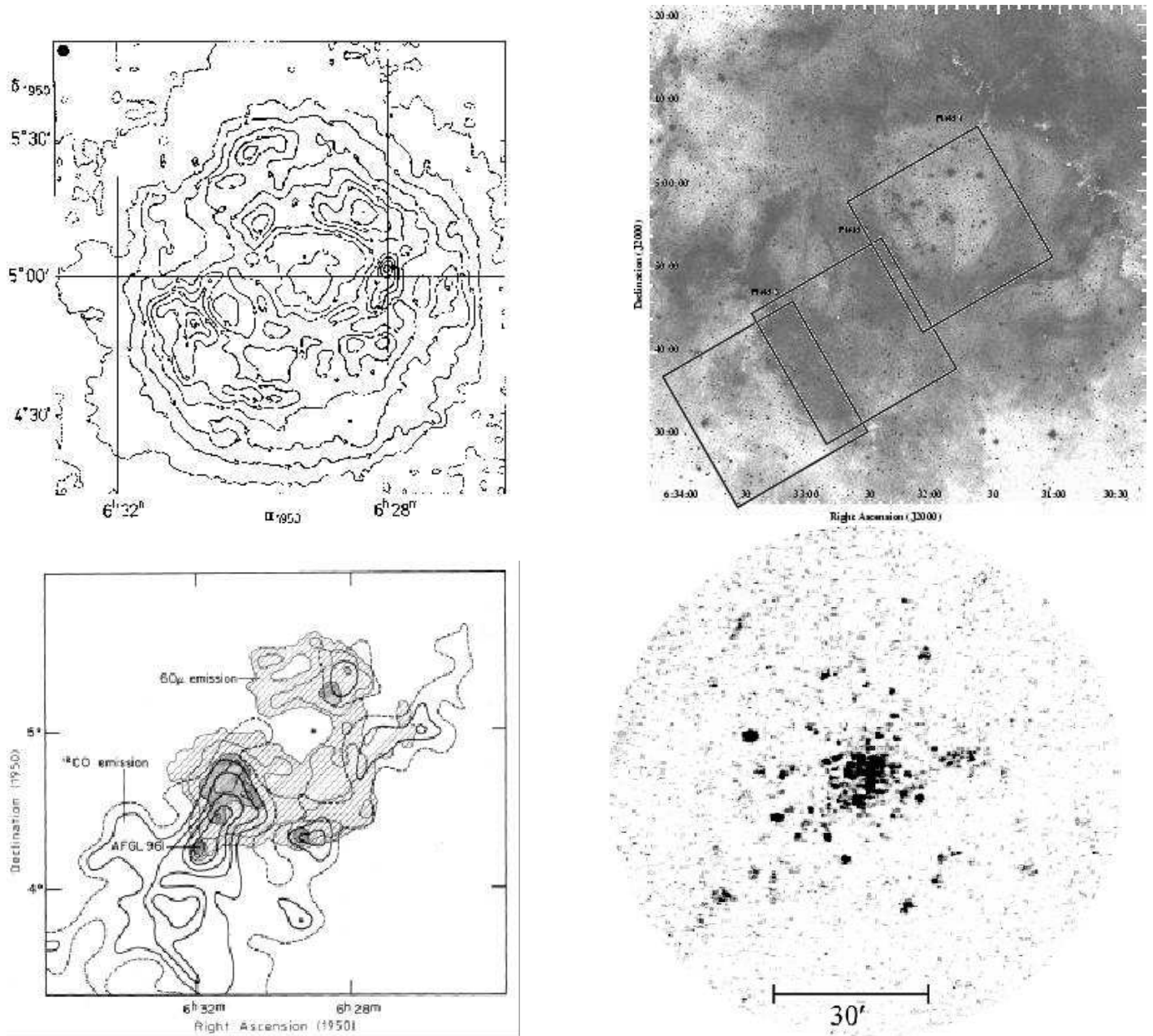


FIG. 2.— Multiwavelength views of the Rosette Nebula and Rosette Molecular Cloud (RMC): (a) Radio continuum map showing HII gas, from Celnik (1985); (b) Digitized Sky Survey image of the Rosette Nebula with overlays showing the approximate locations of the first three ACIS-I fields; (c) contour map of molecular CO in the RMC with $60\mu\text{m}$ IRAS emission superposed and the central cluster marked by an asterisk, from Cox, Deharveng, & Leene (1990); (d) ROSAT PSPC X-ray image of the open cluster NGC 2244, from Berghöfer & Christian (2002).

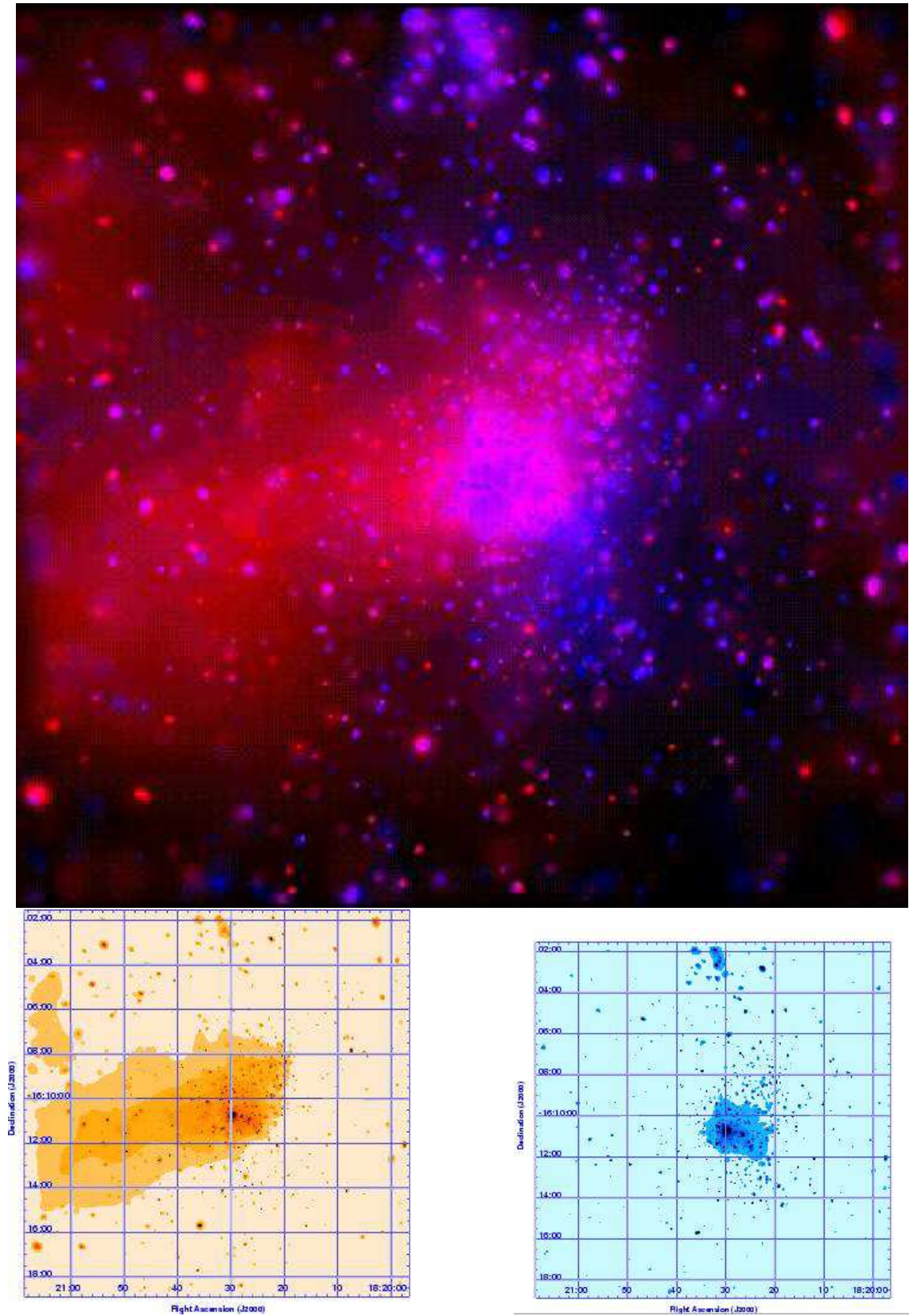


FIG. 3.— (a) *Chandra* ACIS-I image of M 17 with *csmooth* adaptive smoothing and exposure correction (2.07 pixels per bin). Red intensity is scaled to the soft (0.5–2 keV) emission and blue intensity is scale to the hard (2–8 keV) emission. (b) The smoothed 0.5–2 keV image used for the red intensity in (a), highlighting the soft diffuse emission. (c) The smoothed 2–8 keV image used for the blue intensity in (a), highlighting the hard emission.

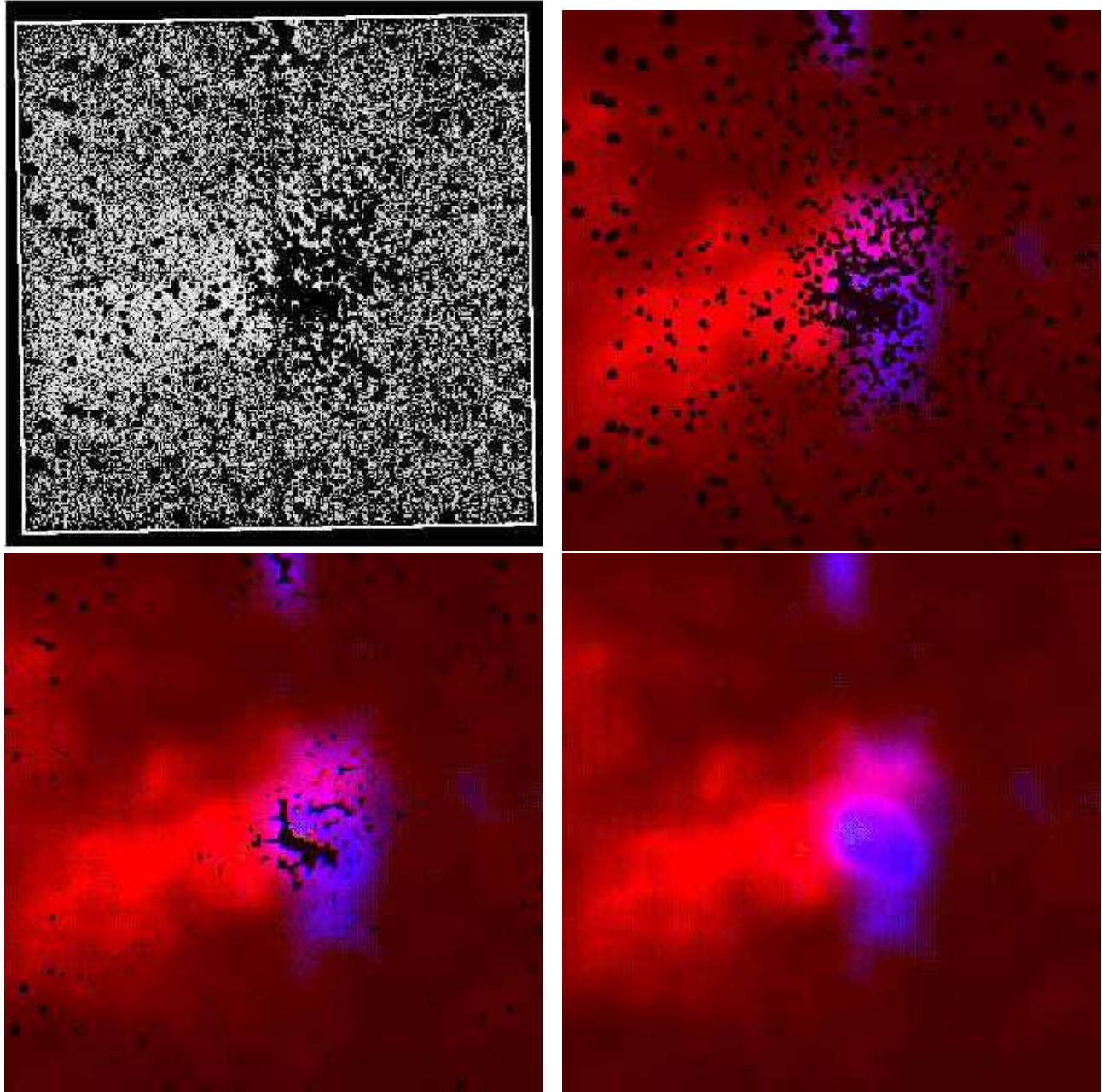


FIG. 4.— (a) *Chandra* ACIS-I binned image (8×8 pixels) of M 17, 0.5–7 keV, with the > 900 detected point sources removed for the study of diffuse emission. See §3 for details. The gaps between the 4 CCDs in the ACIS-I array are faintly visible. (b) *Chandra* ACIS-I swiss-cheese (sources-removed) image of M 17 using our own adaptive smoothing algorithm and exposure correction (8 pixels per bin). Red intensity is scaled to the soft (0.5–2 keV) emission and blue intensity is scale to the hard (2–7 keV) emission. (c) The same datasets as in (b) with the holes partially smoothed over. (d) The same datasets as in (b) with the holes completely smoothed over. The three smoothed images use identical intensity scaling.

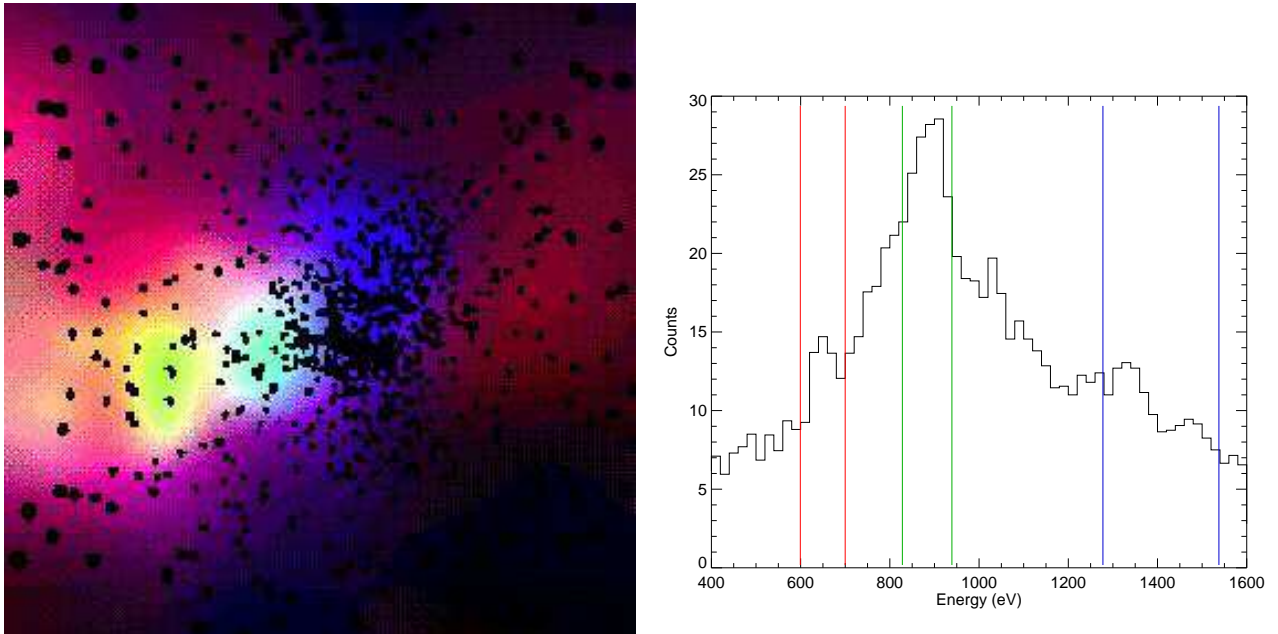


FIG. 5.— (a) A three-color image of the smoothed soft diffuse emission in M 17: red = 600–700 eV, 1267 events; green = 830–940 eV, 2871 events; blue = 1280–1540 eV, 2623 events. (b) A spectrum of the soft diffuse emission, binned at a constant 20 eV per bin to show the peaks in the emission that were used to define the three soft bands for (a). Vertical bars delineate the bands.

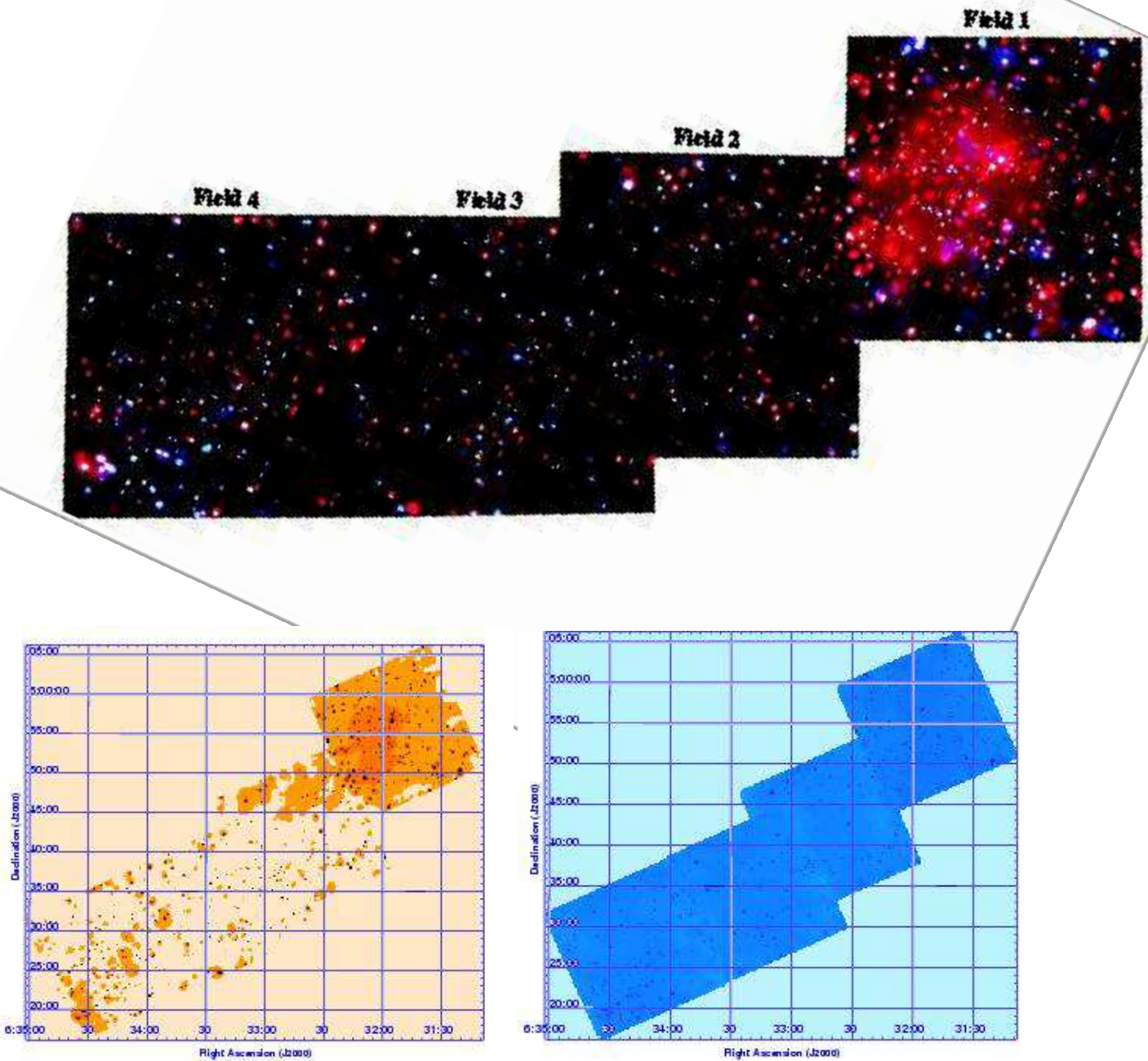


FIG. 6.— (a) *Chandra* ACIS-I $1^\circ \times 0.25^\circ$ mosaic of the Rosette Nebula and RMC, after *csmooth* adaptive smoothing and exposure correction (2.65 pixels per bin). Red intensity is scaled to the soft (0.5–2 keV) emission and blue intensity is scaled to the hard (2–8 keV) emission. This image has been rotated to fit better on the page; the actual orientation of the field on the sky is given in the lower panels. (b) The smoothed 0.5–2 keV image used for the red intensity in (a), highlighting the soft diffuse emission. (c) The smoothed 2–8 keV image used for the blue intensity in (a), showing that there is no significant hard diffuse emission in this field.

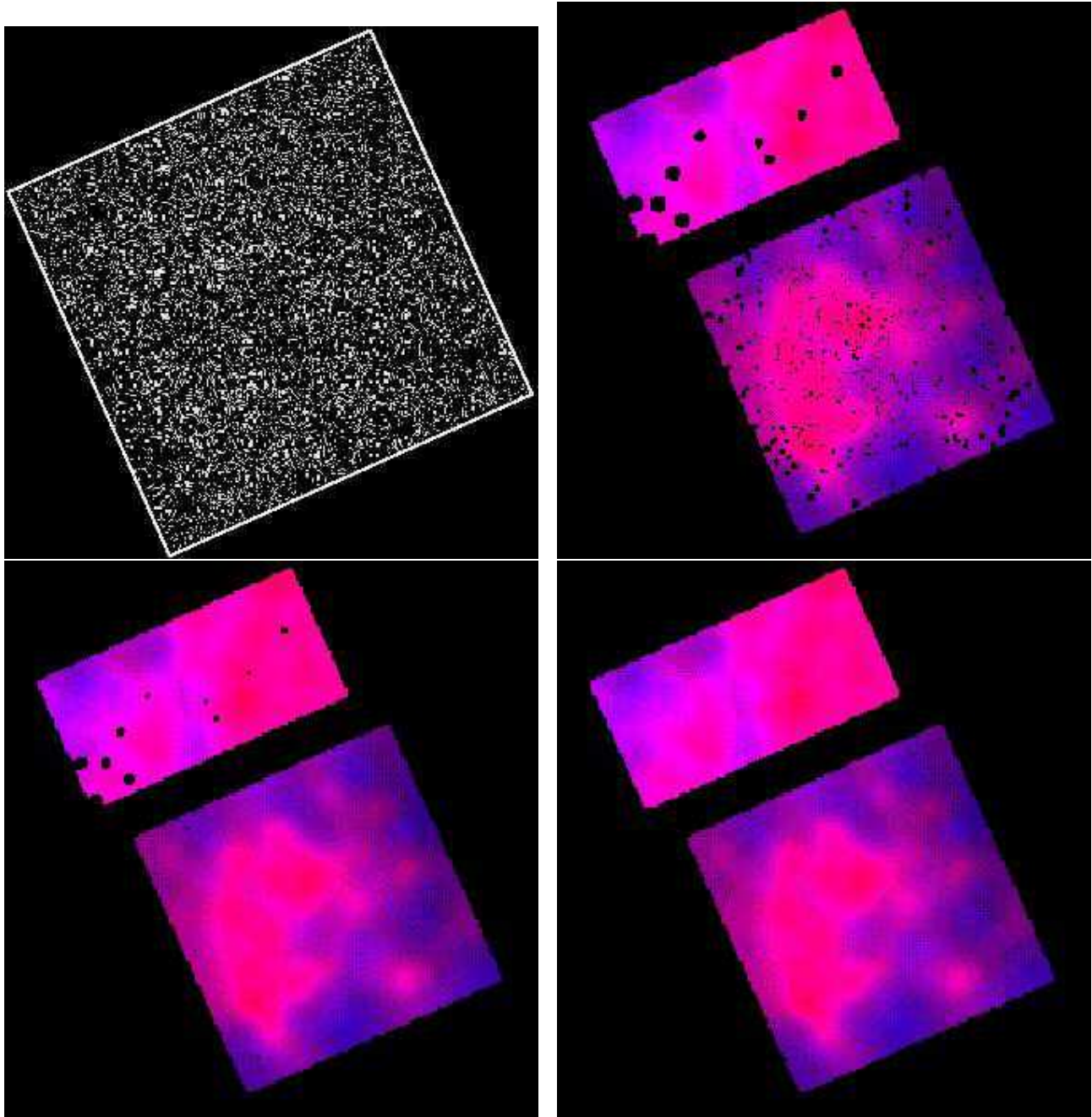


FIG. 7.— (a) *Chandra* ACIS-I binned image (8×8 pixels) of the Rosette Nebula pointing (Field 1, the westernmost of the four pointings in the mosaic in Figure 6a), 0.5–7 keV, with the > 350 detected point sources removed for the study of diffuse emission. See §3 for details. The gaps between the 4 CCDs in the ACIS-I array are faintly visible. (b) *Chandra* ACIS swiss-cheese (sources-removed) image of Rosette using our own adaptive smoothing algorithm and exposure correction (8 pixels per bin). Red intensity is scaled to the soft (0.5–2 keV) emission and blue intensity is scaled to the hard (2–7 keV) emission. The off-axis S2 and S3 chips are included at the top of this image; the background on S3 (a back-illuminated CCD, top right in the image) is higher than the other CCDs, so no information on diffuse emission there can be inferred from this image. (c) The same datasets as in (b) with the holes partially smoothed over. (d) The same datasets as in (b) with the holes completely smoothed over. The three smoothed images use identical intensity scaling.

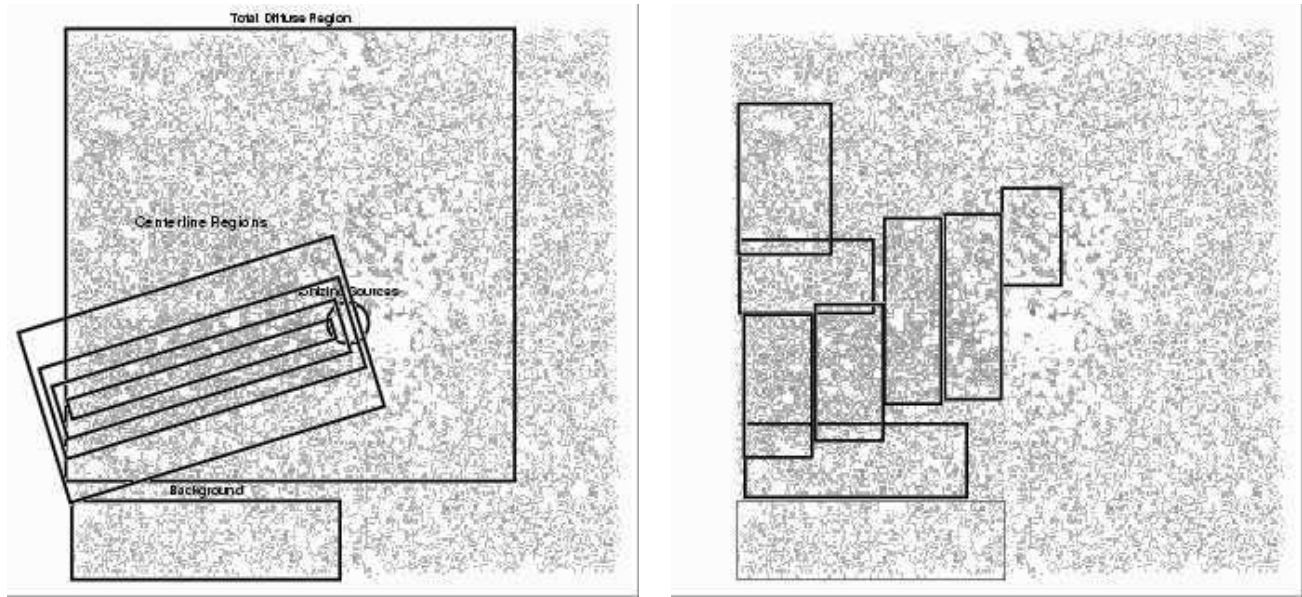


FIG. 8.— Regions used for spectral fitting of diffuse emission in M 17, overlaid on a full-band, binned, sources-removed image of the diffuse emission. (a) Outlined are the large region used for our spectral analysis of the diffuse emission seen in M 17, the region at the bottom of the I1 CCD used as background for that spectral fitting, and the rectangular annuli following the centerline of the soft diffuse emission, used to search for temperature gradients away from the centerline. The circle represents the approximate location of the ring of O stars at the center of NGC 6618. (b) Other regions used to look for temperature variations in the diffuse emission, particularly as a function of distance from the ionizing O stars. The I1 background region is again shown in light outline at the bottom left.

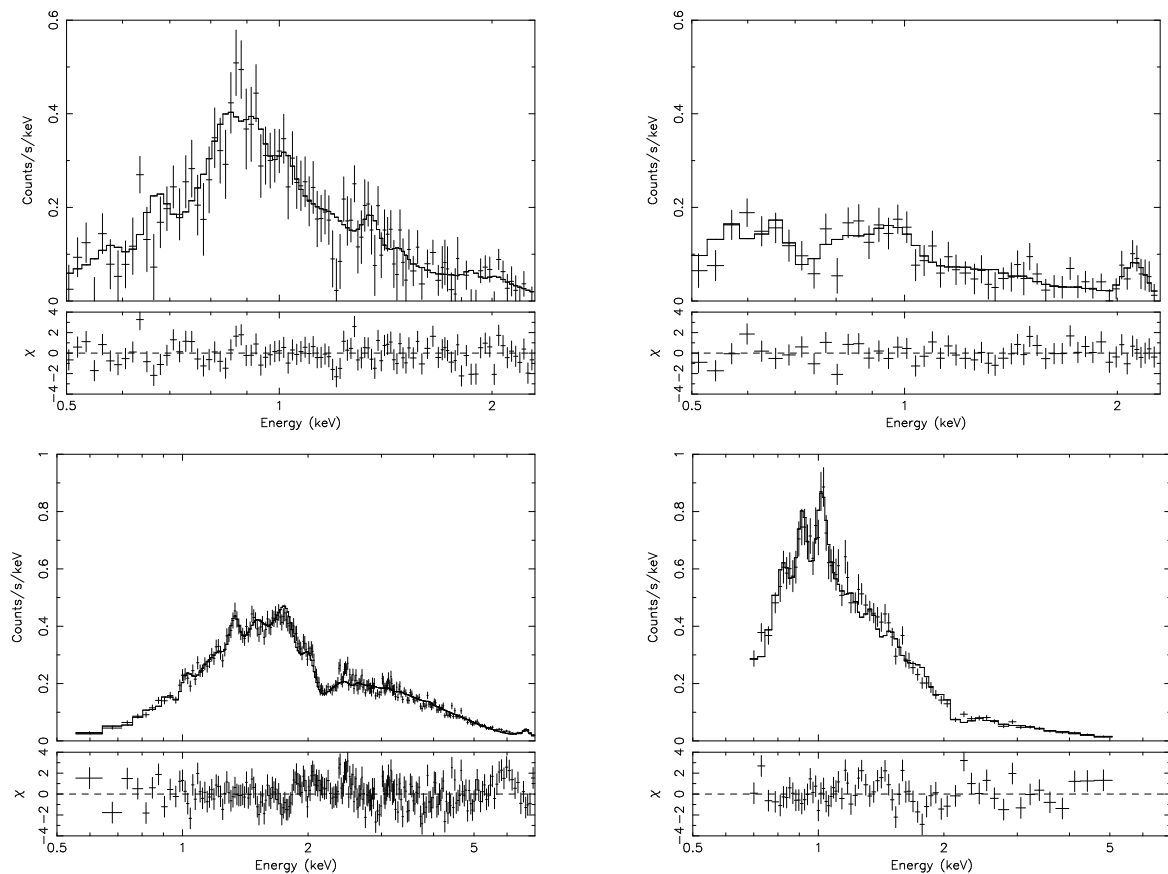


FIG. 9.— ACIS spectra of the following composite components using the spectral models given in Table 2: (a) M 17 diffuse emission; (b) Rosette diffuse emission; (c) M 17 point sources; (d) Rosette point sources. The upper panels show the data and best-fit models; lower panels give the (Data–Model) residuals.

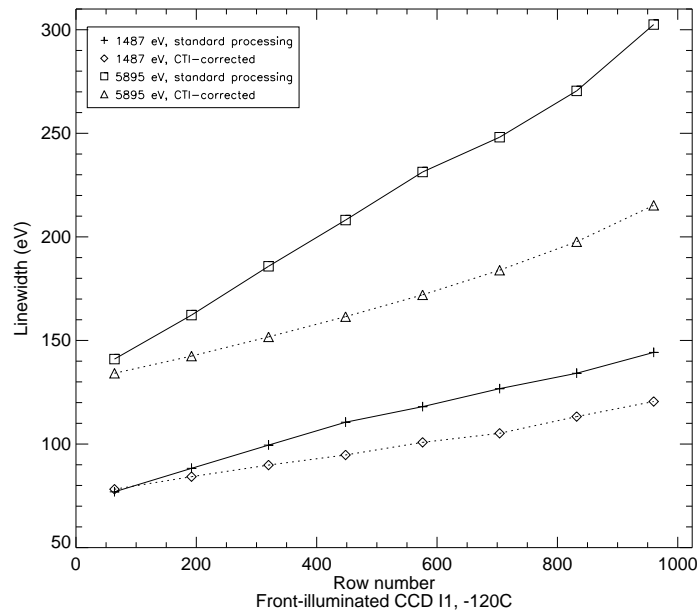


FIG. 10.— ACIS spectral resolution on a front-side illuminated CCD as a function of row number, before and after charge transfer inefficiency (CTI) correction using the PSU algorithm. By reducing the spectral resolution variation across the CCDs, CTI correction substantially improves spectral analysis of diffuse structures on ACIS-I.

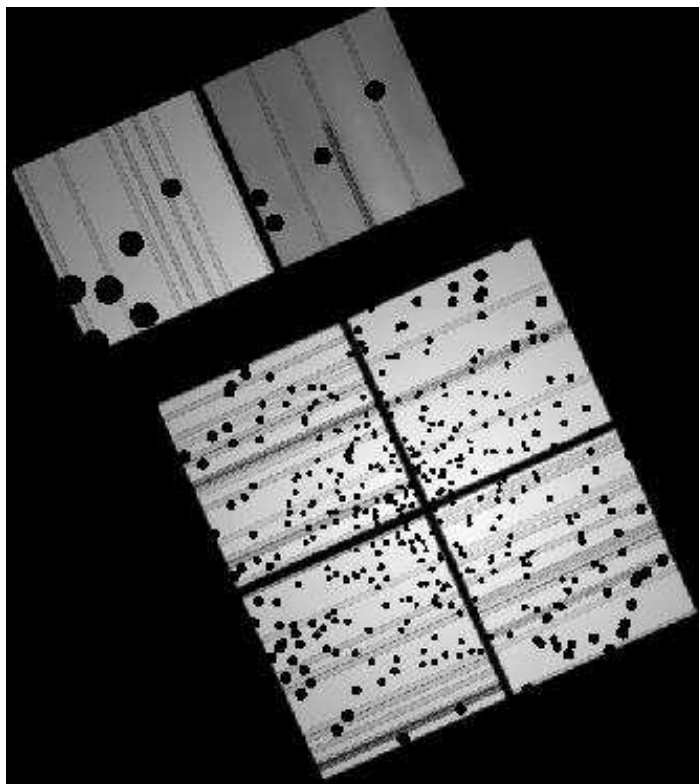


FIG. 11.— An example ACIS-I exposure map, including the ‘swiss-cheese’ masks.

TABLE 1
LOG OF *Chandra* OBSERVATIONS

Target	Date	R.A. (J2000)	Dec (J2000)	Integration (s)
M 17	2 Mar 2002	18 20 30.39	−16 10 29.7	39440
Rosette Field 1	5 Jan 2001	06 31 52.85	+04 55 42.0	19700
Rosette Field 2	5 Jan 2001	06 32 40.84	+04 42 45.0	19500
Rosette Field 3	5 Jan 2001	06 33 17.15	+04 34 42.0	19410
Rosette Field 4	6 Jan 2001	06 34 17.34	+04 27 45.9	19510

Note. — Positions are for the ACIS Imaging Array aimpoint. The exposure time is the net usable time after various filtering steps are applied in the data reduction process.

TABLE 2
X-RAY SPECTRA AND LUMINOSITIES

Target	Counts	Scaled Bkgd Counts	Absorption ^a		Plasma Temp (keV)		Gaussians (keV)	X-ray Luminosities ^b				reduced χ^2
			$N_{H,1}$	$N_{H,2}$	kT_1	kT_2		L_{soft}	L_{soft}^c	L_{hard}	L_{hard}^c	
M 17 diffuse	19,700	~ 9700	4 ± 1	...	0.13 ± 0.02	0.6 ± 0.1	2.1	0.4	3.4	1.2
Rosette diffuse	7800	~ 4500	2 ± 1	...	0.06 ± 0.02	0.8 ± 0.1	2.1	0.2	0.6	0.7
M 17 pt srcs	36,600	...	7 ± 1	17 ± 1	0.19 ± 0.02	3.0 ± 0.1	1.1, 1.3, 6.7	0.6	6.1	3.5	4.1	1.5
Rosette pt srcs	9500	...	6 ± 1	...	0.20 ± 0.02	2.1 ± 0.2	...	0.6	7.4	0.6	0.7	1.6

^ain units of 10^{21} cm^{-2}

^bin units of $10^{33} \text{ ergs s}^{-1}$

TABLE 3
PHYSICAL PROPERTIES OF THE HII REGION PLASMAS

Parameter	Scale factor	M 17	Rosette
<i>Observed X-ray properties</i>			
kT_x (keV)	...	0.6	0.8
$L_{x,bol}$ (ergs s ⁻¹)	...	4×10^{33}	8×10^{32}
V_x (cm ³)	η	9×10^{56}	9×10^{56}
<i>Derived X-ray plasma properties</i>			
T_x (K)	...	7×10^6	9×10^6
$n_{e,x}$ (cm ⁻³)	$\eta^{-1/2}$	0.3	0.1
P_x/k (K cm ⁻³)	$\eta^{-1/2}$	5×10^6	2×10^6
E_x (ergs)	$\eta^{1/2}$	9×10^{47}	3×10^{47}
τ_{cool} (yr)	$\eta^{1/2}$	7×10^6	1×10^7
M_x (M _⊙)	$\eta^{1/2}$	0.15	0.04
<i>Derived photodissociation region properties</i>			
$n_{e,II}$ (cm ⁻³)	...	10^3	10^3
T_{II} (K)	...	8000	6400
P_{II}/k (K cm ⁻³)	...	1×10^7	9×10^6
<i>O star wind properties</i>			
Stellar age t_* (yr)	...	1×10^6	2×10^6
$\Sigma(\dot{M}_w)$ (M _⊙ yr ⁻¹)	...	3×10^{-5}	1×10^{-5}
$\Sigma(\dot{M}_w)t_*$ (M _⊙)	...	30	20
E_w (ergs)	...	9×10^{48}	2×10^{48}

Note. — η is a multiplicative factor for the volume of the emitting plasma, correcting the observed volume to the actual volume, taking extinction, possible inhomogeneities, etc. into account. Note that all derived plasma properties, being $\propto \eta^{1/2}$, are not very sensitive to this correction. See §5.3 for details.

TABLE 4
DIFFUSE X-RAYS FROM HIGH MASS STAR FORMING REGIONS (HMSFRS)

Region	Distance (pc)	Earliest Star ^a	# O6 or earlier	Diffuse X-rays?	Diffuse Area (pc ²)	N_H 10^{21} cm ⁻²	kT (keV)	L_x^b 10^{33} ergs s ⁻¹	Ref.
LMSFRs ^c	150-350	late B	0	no	$\leq 10^{-5}$...
Orion Nebula	450	O6	1	no	$< 10^{-3}$	1
Eagle Nebula	2000	O5	2:	$< 10^{-3}$	2
Lagoon – NGC 6530	1800	O4	3:	no	$< 10^{-2}$	3
Lagoon – Hourglass	1800	O7	0	probably	0.04	11.1	0.63	$\leq 0.7^d$	3
Rosette Nebula	1400	O4	2	yes	47	2	0.06, 0.8	$\leq 0.6^d$	4
RCW 38	1700	O5	1:	yes	2	11.5 ^e	2.2 ^e	1.6 ^e	5
Omega Nebula ^f	1600	O4	7	yes	42	4	0.13, 0.6	3.4	4
Arches Cluster	8500	O3/W-R	>30	yes	14	100	5.7	16	6
NGC 3603	7000	O3/W-R	>20	yes	50	7	3.1	20	7
Carina Nebula	2300	O3/W-R	>30	yes	1270	3–40	0.8:	200:	8

^aSome of these regions contain heavily obscured ultra-compact HII regions or high-mass protostars, so the “earliest star” is approximate. We list here the earliest spectral type given in the literature.

^bLuminosities are obtained from the listed reference. They are corrected for absorption and usually cover the 0.5–2 keV band for soft emission, the 2–8 keV band for hard emission. For diffuse emission that extends beyond the ACIS-I FoV, these are lower limits. The X-ray luminosity in LMSFRs refers to two cases of diffuse X-rays from Herbig-Haro outflow shocks.

^cLow-mass star formation regions near the Sun such as the Taurus-Auriga, Ophiuchi, Chamaleon, Lupus and Perseus clouds. Very faint and localized regions of diffuse X-rays have been found in two young stellar outflows; see text.

^dThe upper limits here refer to likely contributions from unresolved stellar X-ray sources.

^eThermal plasma fit to the core of the diffuse emission; the authors prefer a power law plus thermal plasma fit, with $N_H = 9.5 \times 10^{21}$ cm⁻², $\Gamma = -1.6$, and $kT = 0.2$ keV for the total diffuse emission. We estimated L_x from these parameters using PIMMS (<http://xte.gsfc.nasa.gov/Tools/w3pimms.html>).

^fValues for area, N_H , kT , and L_x are determined from the ACIS data. Additional diffuse soft X-rays are seen in the *ROSAT* data, outside the ACIS field of view; including this emission would roughly double the area and increase L_x by $\sim 1 \times 10^{33}$ ergs s⁻¹ (Dunne03).

References. — 1: Feigelson et al. (2002); 2: Mytyk et al. (2001); 3: Rauw et al. (2002); 4: this work; 5: Wolk et al. (2002); 6: Yusef-Zadeh et al. (2002); 7: Moffat et al. (2002); 8: Seward & Chlebowski (1982).

TABLE 5
O AND EARLY B STARS IN NGC 6618 (M 17 CLUSTER)

CEN	Name ^a			R.A. (J2000) ^b	Dec (J2000) ^b	Spectral Type ^c	ACIS detected?
	B	OI					
37	174	18 20 30.54	-16 10 53.3	O3-O6	yes
43	137	18 20 33.14	-16 11 21.6	O3-O4	yes
1	189	341	...	18 20 29.92	-16 10 45.5	O4+O4 ^d	yes
102	305	780	...	18 20 23.05	-16 07 58.9	O5	no
2	111	337	...	18 20 34.55	-16 10 12.1	O5	yes
...	...	345	...	18 20 27.52	-16 13 31.8	O6	yes
18	260	326	...	18 20 25.94	-16 08 32.3	O7-O8	yes
25	164	18 20 30.92	-16 10 08.0	O7-O8	yes
34	358	715	...	18 20 21.48	-16 10 00.0	O8	no
16	311	258	...	18 20 22.76	-16 08 34.3	O9-B2	yes
61	181	18 20 30.30	-16 10 35.2	O9-B2	yes
3 ^e	98	342	...	18 20 35.47	-16 10 48.9	O9	yes
31	289	18 20 24.45	-16 08 43.3	O9.5	yes
51	243	18 20 26.64	-16 10 03.7	early B	no ^f
92	331	770	...	18 20 21.77	-16 11 18.3	B0	no
28	150	18 20 31.92	-16 11 38.6	B0	yes
57	269	736	...	18 20 25.59	-16 11 16.3	B1	yes
95	266	773	...	18 20 25.72	-16 08 59.1	B1	no
101	206	779	...	18 20 29.04	-16 11 10.5	B1	yes
97	204	775	...	18 20 29.31	-16 09 43.3	B1	yes
100	159	778	...	18 20 31.25	-16 09 29.9	B1	yes
45	18 20 35.6	-16 10 53	B1	no
33	324	714	...	18 20 22.19	-16 09 19.5	B2	no
24	275	18 20 25.11	-16 10 26.7	B2	no
49	268	18 20 25.35	-16 10 19.2	B2	no
48	248	18 20 26.31	-16 10 16.4	B2	no
90	241	768	...	18 20 26.91	-16 10 58.8	B2	yes
85	223	763	...	18 20 28.29	-16 10 49.8	B2	yes
84	207	762	...	18 20 29.01	-16 10 42.5	B2	no
96	...	774	...	18 20 29.2	-16 09 39	B2	no
89	190	767	...	18 20 29.88	-16 10 11.5	B2	no
99	152	777	...	18 20 31.83	-16 09 46.2	B2	yes
17	336	269	...	18 20 21.40	-16 11 40.7	B3	yes
93	337	771	...	18 20 21.43	-16 10 41.2	B3	yes
35	333	716	...	18 20 21.54	-16 09 39.4	B3	yes
75	308	754	...	18 20 22.98	-16 08 14.8	B3	no
94	299	772	...	18 20 23.76	-16 10 35.8	B3	no
91	282	769	...	18 20 24.76	-16 11 09.0	B3	yes
83	267	761	...	18 20 25.63	-16 10 54.1	B3	yes
14	254	703	...	18 20 26.09	-16 10 51.5	B3	no
26	253	18 20 26.13	-16 11 05.1	B3	yes
74	245	753	...	18 20 26.77	-16 08 22.9	B3	no
46	230	726	...	18 20 27.89	-16 11 02.5	B3	yes
47	227	727	...	18 20 28.07	-16 11 09.3	B3	no
65	220	744	...	18 20 28.32	-16 09 58.5	B3	no
27	197	708	...	18 20 29.93	-16 11 37.6	B3	yes
44	18 20 30.4	-16 10 05	B3	no
50 ^g	...	730	...	18 20 26.35	-16 10 19.0	B3	no
58 ^g	18 20 22.45	-16 10 17.3	B3	no
81 ^h	B3	...
82 ^g	...	760	...	18 20 25.56	-16 10 55.1	B3	yes

^aCEN = Chini, Elsaesser, & Neckel (1980); B = Hanson, Howarth, & Conti (1997) derived from Bumgardner (1992); OI = Ogura & Ishida (1976).

^bPositions are from Hanson, Howarth, & Conti (1997); Chini & Wargau (1998), or SIMBAD.

^cSpectral types from Hanson, Howarth, & Conti (1997) or Chini, Elsaesser, & Neckel (1980); assumed to be Luminosity Class V.

^dThe O4–O4 binary Kleinmann’s Anonymous Star; see §2.1.

^eBD -16°4818

^fSource lies in gap between ACIS CCD chips.

^gPositions provided by R. Chini, private comm.

^hPosition unavailable, so no X-ray match can be made.

TABLE 6
O AND EARLY B STARS IN NGC 2244 (ROSETTE CLUSTER)

HD/BD	Name ^a		R.A. (J2000) ^b	Dec (J2000) ^b	Spectral Type ^c	ACIS detected?
	J	OI				
46223	3	203	06 32 09.32	+04 49 24.9	O4 V((f))♡	yes
46150	2	122	06 31 55.53	+04 56 34.5	O5 V((f))♡	yes
46485	...	387	06 33 50.96⊠	+04 31 31.6⊠	O7 V ◊	yes ^e
46056	7	84	06 31 20.88	+04 50 04.0	O8 V((f))	yes
46149	4	114	06 31 52.54	+05 01 59.4	O8.5 V((f))	yes
258691	...	376	06 30 33.33	+04 41 27.9	O9 V((f))	not in FoV
46202	6	180	06 32 10.48	+04 58 00.1	O9 V((f))	yes
259238	19	239	06 32 18.21◊	+05 03 21.7◊	B0 V ◊	not in FoV
46106	5	115	06 31 38.40	+05 01 36.6	B0.2 V	yes
*	06 31 37.10	+04 45 53.7	B0.5 V	not in FoV
259135†	8	200	06 32 00.62	+04 52 41.1	B0.5 V ^d	yes
*♠	06 33 37.51	+04 48 47.0	B0.5 V	not in FoV
259012	9A	80	06 31 33.48	+04 50 40.0	B1 V	yes
259105	10	128	06 31 52.02	+04 55 57.5	B1 V	no
+04° 1299s	11	201	06 32 06.15	+04 52 15.6	B1 III	yes
46484	...	389	06 33 54.41⊠	+04 39 44.6⊠	B1 V ◊	not in FoV
+05° 1281B	14	193	06 31 58.95	+04 55 40.1	B1.5 V	yes
259172	16	167	06 32 02.59	+05 05 08.9	B2 V	not in FoV
...	...	345	06 33 06.58◊	+05 06 03.4◊	B2 ◻	not in FoV
+04° 1295p	15	79	06 31 31.48	+04 51 00.0	B2.5 V	no
...	27	130	06 31 47.90	+04 54 18.3	B2.5 V◊	no
...	23	190	06 31 58.92◊	+04 56 16.1◊	B2.5 Vn◊	no
...	22	172	06 32 09.9△	+05 02 14△	B2.5 V◊	no
*	...	274	06 32 24.24	+04 47 04.0	B2.5 V	no ^f
*	...	392	06 33 50.56	+05 01 37.8	B2.5 V	not in FoV
...	33	194	06 32 15.48	+04 55 20.2	B3 ◻	yes
*	06 32 22.49	+04 55 34.4	B3 V	yes
259268	20	241	06 32 23.05◊	+05 02 45.7◊	B3 ◻	not in FoV
259300	17	253	06 32 29.40	+04 56 56.3	B3 Vp◊	yes
...	...	334	06 32 51.79◊	+04 47 16.1◊	B3 ◻	yes ^f
*	06 33 10.16	+04 59 50.2	B3 V	not in FoV

^aJ = Johnson (1962); OI = Ogura & Ishida (1981); * = Massey, Johnson, & Degioia-Eastwood (1995); † = V578 Mon; ♠ = IRAS 06309+0450.

^bPositions from Massey, Johnson, & Degioia-Eastwood (1995) except those marked with ⊠ from *Hipparcos*, ◊ from Ogura & Ishida (1981), and △ from Park & Sung (2002).

^cSpectral types from Massey, Johnson, & Degioia-Eastwood (1995) except those marked with ♡ from Walborn et al. (2002), ◊ from Ogura & Ishida (1981), and ◻ from Kuznetsov et al. (2000).

^dDouble star

^eObserved in Rosette Field 4.

^fObserved in Rosette Field 2.